Evaluation of aerosol optical depths and clear-sky radiative fluxes of the CERES Edition 4.1 SYN1deg data product

David W. Fillmore[1], David A. Rutan[2], Seiji Kato[3], Fred G. Rose[2],

and Thomas E. Caldwell[2]

[1]University Center for Atmospheric Research, Boulder, CO. 80307, USA

[2]SSAI, Hampton, VA, 23666, USA

[3]NASA Langley Research Center, Hampton, VA, 23666, USA

Submitted to

Atmospheric Chemistry and Physics

April 2021

Corresponding author address: David W Fillmore,
University Center for Atmospheric Research
P.O. Box 3000
Boulder, CO 80307
E-mail: david.w.fillmore@ucar.edu

Abstract

Aerosol optical depths (AOD) used for the Edition 4.1 Clouds and the Earth's Radiant Energy System (CERES) Synoptic (SYN1deg) are evaluated. AODs are derived from Moderate Resolution Imaging Spectroradiometer (MODIS) observations and assimilated by an aerosol transport model (MATCH). As a consequence, clear-sky AODs closely match with those derived from MODIS instruments. AODs under all-sky conditions are larger than AODs under clear-sky conditions, which is supported by ground-based AERONET observations. When all-sky MATCH AODs are compared with Modern-Era Retrospective Analysis for Research and Applications (MERRA2) AODs, MATCH AODs are generally larger than MERRA2 AODS especially over convective regions (e.g. Amazon, central Africa, and eastern Asia). The difference is largely caused by MODIS AODs used for assimilation. Including AODs with larger retrieval uncertainty makes AODs over the convective regions larger. When AODs are used for clear-sky irradiance computations and computed downward shortwave irradiances are compared with ground-based observations, the computed instantaneous irradiances are 1% to 2% larger than observed irradiances. The comparison of top-of-atmosphere clear-sky irradiances with those derived from CERES observations suggests that AODs used for surface radiation observation sites are larger by 0.01 to 0.03, which is within the uncertainty of instantaneous MODIS AODs. However, the comparison with AERONET AOD suggests AODs used for computations over desert sites are 0.08 larger. The cause of positive biases of downward shortwave irradiance and AODs for the desert sites are unknown.

1. Introduction

Accurate estimates of the radiative effects of clouds and aerosols are essential for an understanding the radiative forcing to the Earth's climate system (Bauer and Menon, 2012, Boucher et al. 2013). In addition, through the reflection and absorption of solar radiation, and the absorption and emission of terrestrial thermal radiation, clouds and aerosols affect the radiative heating of both the atmosphere and the surface, which in turn governs the atmospheric circulation and the hydrological cycle (e.g. Stephens et al. 2020, L'Ecuyer et al. 2015). Under the Earth Observing System (EOS) program, the National Aeronautics and Space Administration (NASA) has placed into orbit a series of satellites devoted to long term observations of the climate state. Among these are Terra and Aqua, the flagship satellites of the EOS. Central to observation of climate evolution are Moderate Resolution Imaging Spectroradiometer (MODIS) and the Clouds and the Earth's Radiant Energy System (CERES) instrument pairs that fly on both the Terra (March 2000 - present) and the Aqua (July 2002 - present) platforms (Wielicki et al. 1996). Additional CERES instruments were launched (October 2011) upon the Suomi National Polar-orbiting Partnership (NPP) satellite along with the MODIS successor, the Visible Infrared Imager Radiometer Suite (VIIRS), and on the NOAA-20 satellite (November 2017). In addition to observations from these satellites, the CERES mission also integrates observations from the Geostationary Operational Environmental Satellites (GOES) (West and East), as well as other geostationary satellites around the globe, for full diurnal coverage of clouds and radiation.

The CERES instruments measure broadband radiances over the solar spectrum (shortwave), the thermal infrared (longwave radiance is obtained from a total channel

minus the shortwave channel), and the near infrared atmospheric window, with frequent on-board calibration. CERES measurements, in conjunction with MODIS information, are used to infer broadband irradiances through empirical angular distribution models (ADMs). Geosynchronous satellite imagery observes the diurnal cycle of clouds, which is not fully sampled by the polar orbiting satellites upon which CERES and MODIS reside.

While top-of-atmosphere (TOA) irradiances are derived from broadband radiances measured by CERES instruments (Loeb et al. 2005; Su et al. 2015), surface and in atmosphere irradiances are computed with a radiative transfer model. Inputs used for the computations include cloud properties derived from MODIS and geostationary satellites, aerosol optical depth derived from MODIS radiances, and surface albedo derived from MODIS and CERES observations (Rutan et al. 2009). Temperature and humidity profiles are provided by a reanalysis product produced by the NASA Goddard Modeling and Assimilation Office (GMAO).

Irradiances at the surface produced by the CERES team have been compared with surface observations (Rutan et al. 2015; Kato et al. 2013, 2018). These comparisons are for all-sky conditions (i.e. including any clouds). Irradiances under clear-sky conditions are not explicitly separated from all-sky conditions in the evaluations. There are several reasons that impede efforts at rigorous validation of clear-sky irradiances with surface observations; 1) a clear-sky condition at a given site does not persist over a long time (e.g. a month or longer), 2) there are mismatches of clear-sky conditions determined by satellite- and ground-based instruments, and 3) field-of-view size between CERES instruments and ground-based radiometers differ.

Despite these difficulties for evaluating computed clear-sky irradiances, clear-sky irradiances play an important role in quantifying aerosol and cloud radiative effects (Loeb and Su 2010; Soden and Chung 2017). Therefore, the uncertainty in surface irradiances need to be understood in order to assess the uncertainty in aerosol and cloud radiative effect. This work is the first attempt by the CERES team to evaluate clear-sky surface irradiances provided by its data products. One of the essential variables in computing clear-sky irradiances is aerosol optical depth. In this paper, we evaluate aerosol optical depth used for irradiance computations in the CERES project and analyze how the error propagates to clear-sky surface irradiances. Computations of surface irradiances provided by Edition 4.1 SYN1deg data products use aerosol optical depth derived by a chemical transport model [The Model for Atmospheric Transport and Chemistry (MATCH, Collins et al. 2001)] that assimilates MODIS-derived aerosol optical depth. In Section 2, we explain in some detail the MATCH aerosol transport. In Section 3, the assimilation of aerosol optical depth in the model is discussed. Sections 4 and 5 compares aerosol optical depths used by the CERES team with, those from MERRA2 and the Aerosol Robotic Network (AERONET, Holben et al. 1998).

2. Description of MATCH model

The Model for Atmospheric Transport and Chemistry (MATCH) is a transport model of intermediate complexity driven by offline meteorological fields from the National Centers for Environmental Prediction (NCEP) reanalysis. It is run on a 194×96 (1.9°×1.9°) spatial grid with a vertical resolution of 28 sigma-p levels. Temporally, the meteorological fields are linearly interpolated to 30-minute times at which time the

chemical processes are run. One exception is that the sulfur model is interpolated again to run at 2-min subscale time steps. MATCH is one of the many aerosol transport models that participated in the AeroCom model inter-comparison project (Textor et al., 2006; Kinne et al. 2006; Textor et al. 2007) and the AeroCom carbon inter-comparison project (Koch et al., 2009; Huneeus et al., 2011).

Aerosol types included in MATCH are dust, sulfate, sea salt, soot, sulfates, carbon, and volcanic particles (**Table 1**). Model physics included in MATCH are parameterizations for convection and boundary layer processes that include prognostic cloud and precipitation schemes for aqueous chemistry and the scavenging of soluble species. MATCH also includes the ability to resolve the transport of aerosols via convection, boundary layer transport, and scavenging and deposition of soluble gases and aerosols. MATCH can simulate most cloud processes currently in use in a GCM (eg. cloud fraction, cloud water and ice content, fraction of water converted to rain and snow, and evaporation of condensate and precipitate). It also includes vertical turbulent eddy processes. These processes are then used for convective transport, wet scavenging, wet deposition and dry deposition of the MATCH aerosols. These various parameterizations were developed, originally, for the NCAR Community Climate Model (CCM) and subsequently incorporated into the MATCH model. Descriptions of these parameterizations are given by Rasch et. al (1997, 2001), Collins et. al (2001) and additional papers described therein.

The MATCH aerosol suite includes a detailed mineral dust scheme in the Dust Entrainment and Deposition model, (Zender et al., 2003), and a diagnostic parameterization for sea-salt aerosol based on the 10m wind speed (Blanchard and

141 Woodcock, 1980). The sulfur cycle and the chemical reactions for sulfate aerosol creation
142 rely on monthly climatological oxidant fields and emission inventories (**Table 1**) for
143 sulfur oxides and oceanic dimethyl sulfide (photochemistry and nitrate aerosol are
144 omitted). The reaction scheme is similar to that of the Model for Ozone and Related
145 Chemical Tracers (MOZART), (Emmons et al., 2010). Carbon aerosols (both organic
146 compounds and soot) evolve with simple mean lifetime e-foldings from surface fluxes
147 specified through natural, biomass burning and fossil fuel burning emission inventories
148 (also monthly climatologies given in **Table 1**).
149

Table 1. Aerosol Types & Climatological Sources

Aerosol Type	*Source*	*Description*
Sea Salt	Blanchard and Woodcock, 1980	Wind Driven
Dust	Ginoux et al. (2001); Zender et al. (2003)	NCEP soil moisture, wind driven
Sulfate (natural & anthropogenic)	Benkovitz et al. (1996); Barth et al. (2000)	monthly climatological
Carbon (organic & Soot)	Liousse et al. (1996)	monthly climatological
Volcanic	Episodic inclusion of Sulfur dioxide	Processed by model

150

151 The optical properties of the various aerosol types (e.g. mass extinction
152 coefficient, single scatter albedo), which are key parameters for aerosol assimilation, are
153 drawn from the standard Optical Properties of Clouds and Aerosols (OPAC, Hess et al.
154 1998) database. However, scattering properties of maritime and dust aerosols used
155 in the radiative transfer calculations in the SYN1deg are not from MATCH. Instead,
156 aerosol types from MATCH are mapped to a similar set of scattering properties, per
157 Table 2, embedded in the Langley Fu & Liou radiative transfer (LFLRT) code (Fu and

158 Liou, 1993; Fu et. al 1998; Rose et. al 2013). These include OPAC as in MATCH for all
159 but the small and large dust particles. Dust scattering and absorption properties in the
160 LFLRT code are from Sinyuk et al. (2003).
161

Table 2. Mapping of MATCH aerosol types into Radiative Transfer code.

MATCH Constituent	Langley Fu & Liou Constituent	Langley Fu & Liou Spectral Properties
Sea Salt	Maritime	d'Almeida 1991
Hydrophobic Organic Carbon	Insoluble	OPAC
Hydrophilic Black Carbon Hydrophobic Black Carbon	Soot	OPAC
Hydrophilic Organic Carbon Tropospheric Sulfate	Water Soluble (WASO)	OPAC
Volcanic Stratospheric Sulfate	Suspended Organic (SUSO)	OPAC
Dust < 1.0μm	"Small" Dust	Sinyuk et al. (2003)
Dust 1.0 -2.5μm Dust 2.5-5.0 μm Dust 5.0-10.0 μm	"Large" Dust	Sinyuk et al. (2003)

162

163 **Figure 1** shows the single scatter albedo (SSA) and asymmetry parameter (ASY)
164 for the seven constituents in the LFLRT code at 500μm. Constituents with constant SSA
165 and/or ASY are given as numbers while those that vary with relative humidity are
166 plotted. The spectral properties for sea salt shown in Figure 1 were taken directly from
167 tables in d'Almeida et al., (1991). Note that the asymmetry parameter of maritime
168 aerosol decreases with humidity. This is likely an error in the original Table A.30 of
169 d'Almeida et al. (1991).

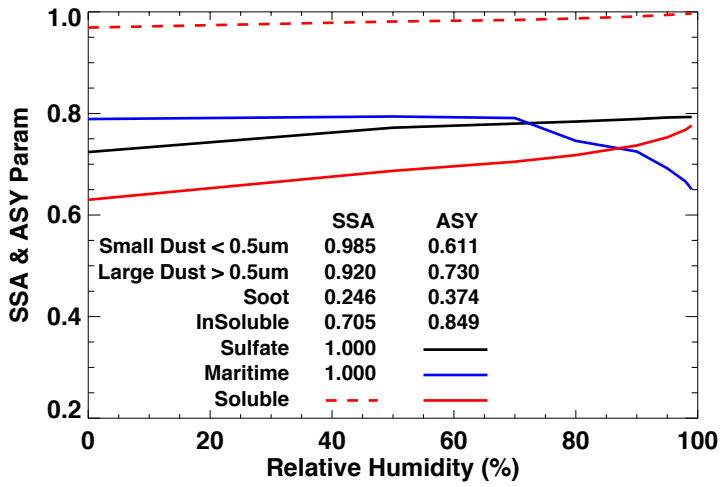

Figure 1. Single scatter albedo and asymmetry parameter for the seven aerosol types available in the Langley Fu & Liou Model SYN1deg calculations. Only those that vary with relative humidity are plotted. Others are listed as constants. All values are for properties at 550 μm.

2.1 MATCH Assimilation of MODIS Aerosol Optical Depths

One major advantage of the MATCH model is its ability to reliably assimilate satellite-based retrievals of aerosol optical depth (AOD) to constrain the climatologically forced aerosols generated within the chemical transport portion of the code. Edition 4 MATCH algorithms ingest MODIS Collection 6.1 AOD (Remer et al., 2005), beginning in March 2000 from the Terra satellite and June 2002 from both Terra and Aqua satellites. The MATCH assimilates MODIS AOD at the green wavelength of 550 nm. MATCH combines AOD derived by the Dark Target (Levy et al. 2013) and Deep Blue algorithms (Hsu et al., 2006). A global daily mean AOD in a 1.9°x1.9° grid is derived from Terra and Aqua observations by simply averaging available Terra and Aqua dark target and deep blue derived AODs in a grid box. Unlike dark target and deep blue

183 merged product (MOD08), we do not use a quality assurance confidence (QAC) score to
184 screen AOD.

185 The assimilation process begins by combining the dark target and deep blue AOD
186 from MODIS (both Terra and Aqua when available) and creating daily averages. As
187 MATCH progresses through time the AOD at local solar noon are assimilated by taking a
188 15° longitude width of retrieved AOD from the daily mean map. Examples of the
189 magnitude of AOD adjustments by the assimilation are shown in **Fig. 2. Figure 2a** shows
190 hourly AOD field differences, 4 UT minus 3 UT on February 1st, 2020. Similarly, **Figure**
191 **2b** shows 10 UT minus 9 UT of the same day. The 15° vertical band is clearly visible
192 where red (blue) colors indicate total column aerosol is increased (decreased) by the
193 MODIS AOD assimilation. Following the AOD adjustment, aerosol masses in the
194 atmospheric column through the troposphere are scaled to closely match the AOD
195 derived from MODIS. Neither the vertical profile nor the relative abundance of the
196 aerosol species is adjusted. Once aerosol mass is adjusted at the local noon for the regions
197 where MODIS AOD is available, the adjusted aerosol mass is carried on to the next time
198 step. Besides the MODIS adjustments, wind driven sea-salt creation and deposition are
199 found along frontal boundaries in the North Atlantic and Southern Oceans. The maps also
200 indicate hourly increases and decreases in high aerosol loading areas such as those found
201 around China and SE Asia.

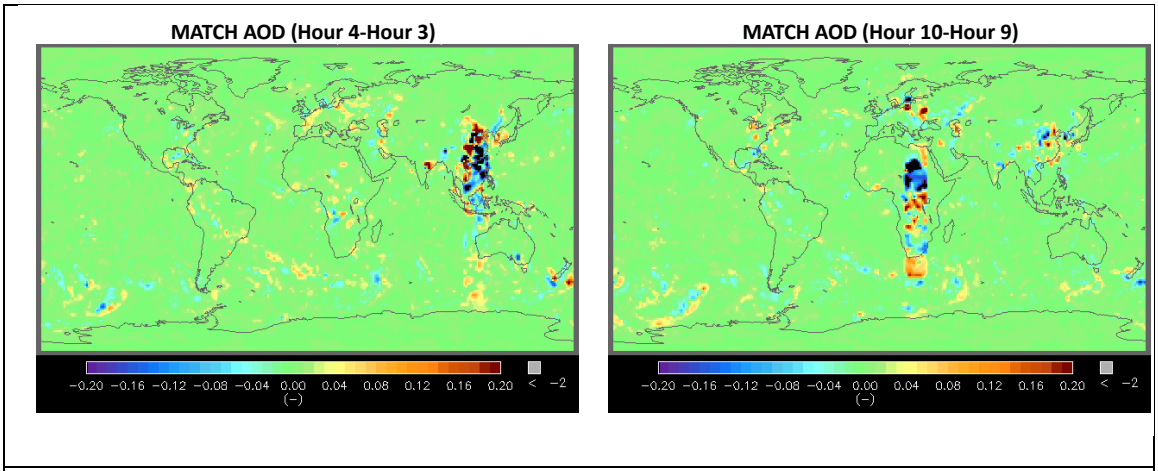

Figure 2. Difference of MATCH AOD due to the assimilation of MODIS AOD. The left plot is 4 UT minus 3 UT and right plot is 10 UT minus 9 UT on February 1, 2020. AOD is adjusted at the local solar noon within the 15° longitudinal band by the MODIS AOD assimilation. Wind-blown dust and sea salts differences are also apparent outside the 15° longitudinal band.

202

203 Episodic events such as intense fires or volcanic eruptions are not specifically
204 included in the MATCH aerosol package. Such events are captured by the assimilation of
205 MODIS AOD and total column aerosol loading is adjusted upward. The adjustment is
206 applied to AOD only. The aerosol type (and so scattering properties) is not adjusted to
207 reflect the reality of the scattering or absorbing aerosol during such an event.

208

209

210 **2.2 MATCH and MERRA2 comparison**

211 In this section, we compare AODs between MATCH and MERRA2 (Randles et
212 al., 2017) in which MODIS clear-sky radiances are assimilated. MERRA2 also
213 assimilates surface observed AOD by AERONET and ship born AOD observations as
214 well as AVHRR and MISR retrievals for the years 2000-2002 and 2000-2014
215 respectively. We compare AODs in two different ways. First, MATCH and MERRA2
216 AODs are compared with MODIS AODs. The first comparison tests the consistency of

daily means when MODIS aerosol optical depth is available (i.e. clear somewhere in the grid box at Terra and Aqua overpass time). Second, MATCH and MERRA2 AODs are compared under all-sky conditions, which is only possible with modeled AODs.

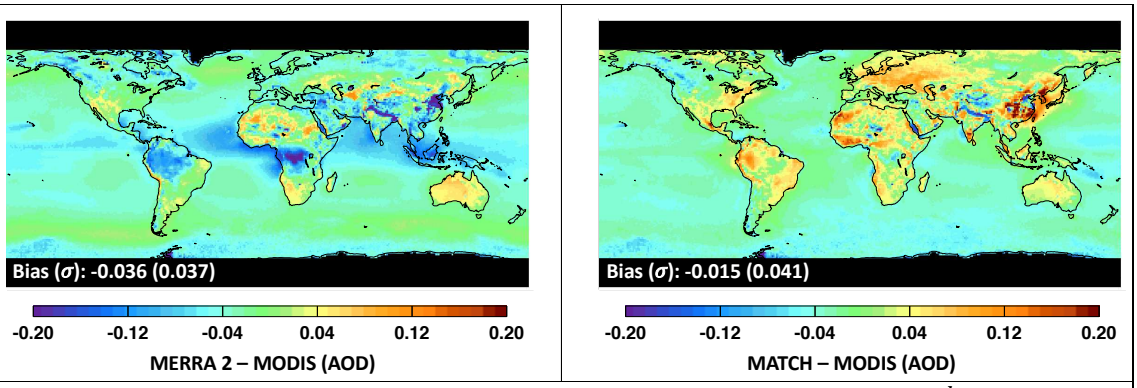

Figure 3: Climatological mean aerosol optical thickens (AOD, i.e. $\langle AOD_{MODIS}^{clr} \rangle$ see texts for the definition) difference of left) MERRA2 – MODIS and right) MATCH – MODIS averaged over Mar 2000 through Feb 2020. MERRA2 and MATCH daily mean AODs are sampled when daily mean MODIS AOD from the same 1°×1° grid is available. Sampled daily mean AODs are subsequently averaged. MODIS AODs are averages of MODIS dark target and deep blue algorithms from both Terra (MOD08) and Aqua (MYD08) data products.

Figure 3 shows differences of climatological mean AOD between MERRA2 and MODIS on the left and MATCH and MODIS on the right. To compute the monthly mean AOD differences, both MERRA2 and MATCH daily mean AODs are sampled when daily mean MODIS AOD (MODIS products MOD08 and MYD08) from the same 1°×1° grid is available (hereinafter AOD_{MODIS}^{clr}). Sampled daily mean AODs (AOD_{MODIS}^{clr}) are subsequently averaged (hereinafter $\langle AOD_{MODIS}^{clr} \rangle$, where the bracket indicates a simple arithmetic mean). Although both products assimilate MODIS observations, each shows fairly significant differences from MODIS values. Differences arise because MODIS daily mean AOD is clear sky at Terra and Aqua overpass time while MERRA2 and MATCH daily mean AOD includes AOD from other times of the day. When the non-overpass time is also clear, MATCH AOD_{MODIS}^{clr} should be close to MODIS AOD_{MODIS}^{clr}.

However, when clouds are present in MATCH during non-overpass times, modeled AOD are used, hence the daily mean AOD can deviate from MODIS AOD_{MODIS}^{clr}. In addition, AOD differences for MERRA2 at Terra and Aqua overpass times might be larger than MATCH even for clear-sky conditions as MERRA2 assimilates observed AOD data other than MODIS AOD when and where these events might occur.

While MATCH shows large positive differences over land, especially China and southeast Asia, Australia, Amazon, and north Africa, MERRA2 shows significant negative differences over major rain-forest regions of south America, Africa, and the tropical western Pacific. Both products are closer to MODIS AOD over ocean compared to $\langle AOD_{MODIS}^{clr} \rangle$ over land except MERRA2 shows a negative difference across the Indian ocean and off the west coast of Africa in the Atlantic Ocean. When MODIS AOD_{MODIS}^{clr} is available in the grid box, MATCH weighs MODIS AOD heavily in its assimilation at local solar noon so that MATCH AOD is nearly identical to MODIS AOD at the local noon under clear-sky regions. Consequently, the difference of climatological global mean MATCH and MODIS AOD_{MODIS}^{clr} (-0.015) is smaller than the difference of MERRA2 and MODIS AOD_{MODIS}^{clr} (-0.036).

Figure 4 shows the difference of AOD_{MODIS}^{clr} more clearly. In **Fig. 4** AOD_{MODIS}^{clr} are compared directly in a log-density plot where each point represents a comparison for the daily average of a given grid box; MERRA2 versus MODIS on the left and MATCH versus MODIS on the right. **Figure 4** indicates that MATCH AOD_{MODIS}^{clr} has a smaller bias with respect to the MODIS AOD than the MERRA2 AOD but has approximately the same RMS compared to the MERRA2 AOD_{MODIS}^{clr}.

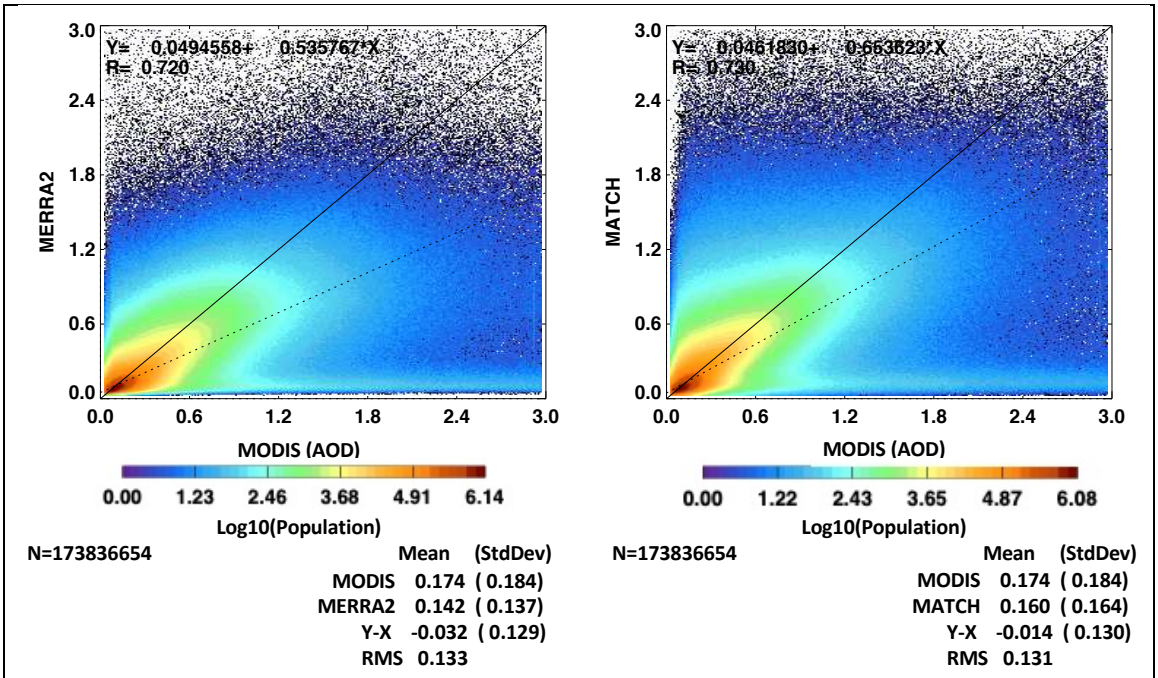

Figure 4: Scatter plot of daily 1°×1° mean aerosol optical depth from a) MERRA2 and b) MATCH versus AOD derived from MODIS on Terra and Aqua for Mar 2000 through Feb 2020. MODIS AODs are 1°×1° daily average of AODs derived by the dark target and deep blue algorithms. Only days and grid boxes that have MODIS AOD (i.e. AOD_{MODIS}^{clr} defined in the texts) are used.

We now consider more directly, differences between the MATCH and MERRA2 climatological AOD fields for all-sky and estimated clear sky conditions. **Figure 5** shows 1°×1° climatological mean maps of MATCH AOD on the left and its difference from MERRA2 on the right for all sky (top maps) and estimated clear sky (bottom maps) conditions for March 2000 through February 2020. A clear-sky area weighted monthly mean aerosol optical depth is derived by averaging daily mean aerosol optical depth weighted by clear fraction (hereinafter $\overline{AOD_{MODIS}^{clr}}$, overbar indicates monthly mean), where the clear fraction is derived from MODIS on Terra and Aqua (Loeb et al. 2020, Minnis et al. 2020). MATCH all-sky AOD (hereinafter $\overline{AOD^{all}}$) is larger than MERRA2 $\overline{AOD^{all}}$), particularly over the rain forest regions of the globe as well as India and China.

Although the difference is smaller, the difference of $\overline{AOD_{MODIS}^{clr}}$ shows a similar spatial pattern (**Fig. 5** bottom right) to the all-sky difference. This is consistent with **Fig. 3**, showing that MERRA2 AOD_{MODIS}^{clr} underestimates AOD with respect to MODIS AOD_{MODIS}^{clr}. A larger difference in MATCH AOD over convective regions (e.g. Amazon, central Africa, and south east Asia) is caused by how dark target and deep blue AOD are merged. As mentioned earlier, we do not use QAC to screen AOD. Convective clouds introduce a larger uncertainty to AOD because of a 3D radiation effect or poor fit to observations with retrieved AOD (personal communication with R. Levy 2020). For these situations, AODs associated with QA confidence scores less than 2 are screened out in the MOD08 dark target and deep blue merged product (Levy et al. 2013).

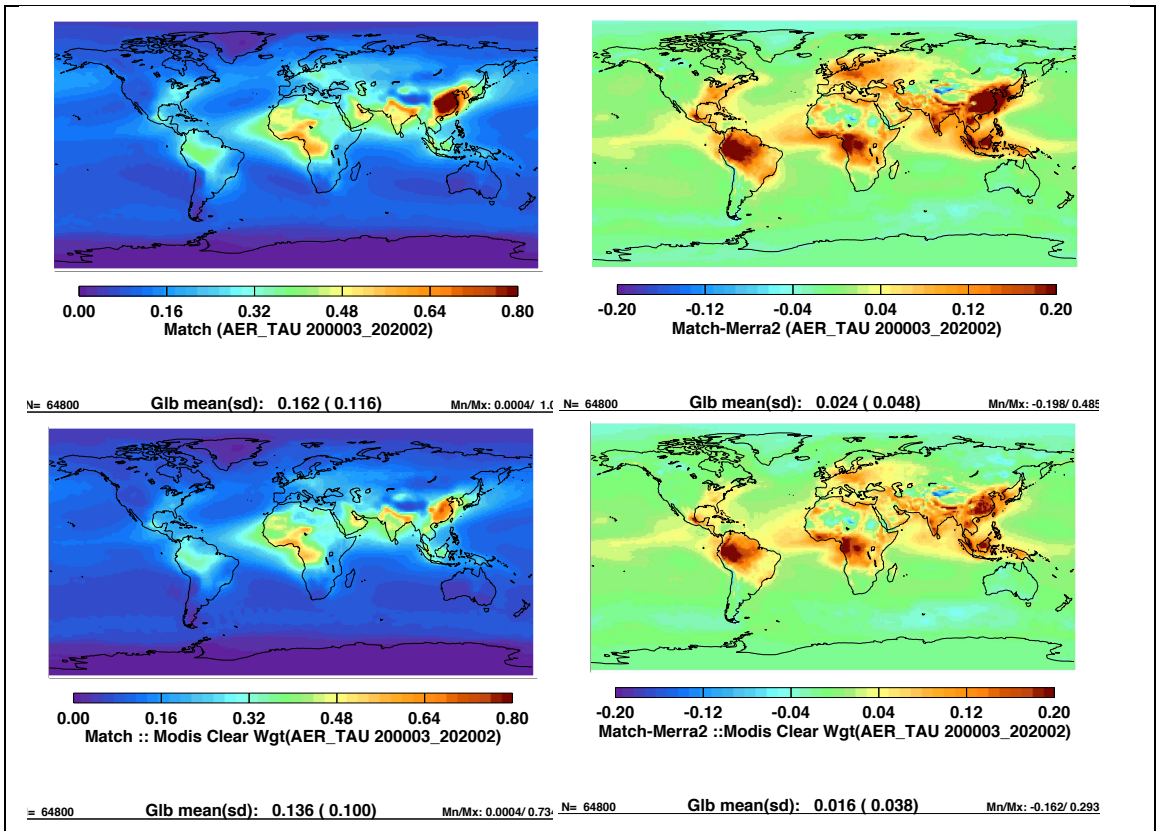

Figure 5. Left) Climatological mean aerosol optical depth from MATCH and right) the difference between MATCH and MERRA2 (MATCH – MERRA2). Top maps are for all-sky (i.e. AOD^{all}_{MODIS}, bottom maps are for clear-sky area weighted average of AOD (i.e. AOD^{clr}_{MODIS}). Clear-sky weighted monthly mean AOD is derived by averaging daily mean aerosol optical depth weighted by daily 1°×1° gridded mean clear fraction where the clear fraction is derived from MODIS based cloud fraction on Terra and Aqua.

2.3 Comparison with AERONET

The above results indicate that both MATCH AOD^{clr}_{MODIS} and MERRA2 $\overline{AOD^{clr}_{MODIS}}$ are generally smaller than MODIS $\overline{AOD^{clr}_{MODIS}}$. Larger difference between MATCH and MERRA2 $\overline{AOD^{all}}$ over convective regions originated from merged AOD product used for the assimilation. Of primary importance to radiative transfer calculations within the SYN1deg product is the ability of the MATCH model to accurately represent total column aerosol optical depth. To test the overall accuracy, we use observations from the AERosol RObotic NETwork (AERONET). AERONET is a global federation of

ground-based remotes sensing sites developed by NASA and now supported by a number of institutions around the world (Holben et al. 1998). Each site maintains a CIMEL sun-photometer that scans the daytime sky every 20 minutes. Collected data are processed according to standards of calibration and processing maintained by the AERONET project. Here we utilize Level 2.0, data that have been screened for clouds and quality assured (Smirnov et al. 2000).

Figure 6 shows an hourly time series of AOD from MATCH, MERRA2 and AERONET for January 2010 at the Beijing China AERONET site. The top plot shows cloud fraction time series derived from MODIS and GEOs from the SYN1deg Ed4.1 product (Rutan et al. 2015), and the bottom plot shows AOD time series. Generally, both models produce a large variability of AOD at this site fairly well over the course of the month. While both MERRA2 and MATCH AODs increase near times when cloud fraction approaches 100%, the increase of MATCH AOD, which correlates with the increase of AERONET AOD relatively well, is larger than the increase of MERRA2 AOD. Although the temporal correlation coefficient of the MATCH and AERONET AODs is smaller at this site during summer months than during winter months (not shown), a good temporal correlation between MATCH and AERONET AODs is consistent across most locations and times we considered. To show this statistically, in the following, we extend this analysis to a number of AERONET sites grouped geographically based on general aerosol type.

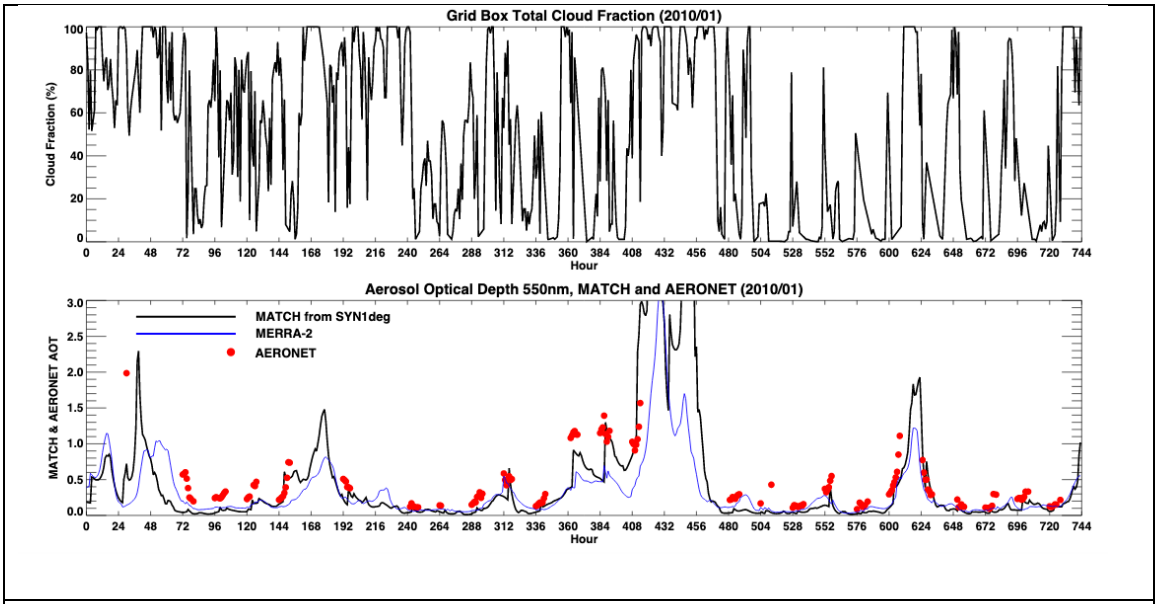

Figure 6. Hourly time series of grid box cloud fraction (top) from SYN1deg Ed4.1 CERES product and Aerosol Optical Depths (bottom). Results from the grid box containing the AERONET Beijing, CH site. Black line MATCH, blue line MERRA-2, red dots, AERONET observations. MATCH and, to a lesser degree MERRA-2 often have large increases in AOD when cloud fraction nears 100%.

311
312

313 Aerosol optical depths from AERONET are nominally provided at 8 spectral
314 channels, every 20 minutes given favorable conditions. We use two channels to derive
315 observed AOD at 550 nm to compare to the AOD provided by the MATCH model.
316 Because the SYN1deg radiative transfer calculation is done hourly, we average any
317 observations within a given hour period centered at the 30th minute for each site
318 collocated within a SYN1deg grid box. AERONET sites chosen are shown in **Fig. 7** with
319 a complete listing of all sites in Appendix 1. Though we examine 55 sites over 20+ years,
320 we aggregate the statistics within continental regions which naturally isolates them by
321 general climatic conditions. Tables 3 and 4 show comparisons for each site grouping,
322 respectively, for clear sky (less than 1% cloud identified by MODIS and geostationary
323 satellites in the SYN1deg grid box) conditions and for all sky (any cloud condition within

the SYN1deg grid box) conditions. Using clear-sky scenes identified by MODIS only gives the same statistical results with fewer number of samples. Statistics shown in Tables 3 and 4 are the average observed value, mean bias (MATCH – Observation), root mean square (RMS) difference and the correlation coefficient (R) over the time period from March 2000 through February 2020. The actual time period varies depending on the site due to AERONET data availability. The RMS difference and correlation coefficient are computed by each site with hourly mean values where observations are available from March 2000 through February 2020. For comparison purposes we show the same statistics derived from observations compared to MERRA2 AODs using the identical hours. We note, however, that MERRA2 assimilates AERONET while MATCH AODs are independent from AERONET AODs.

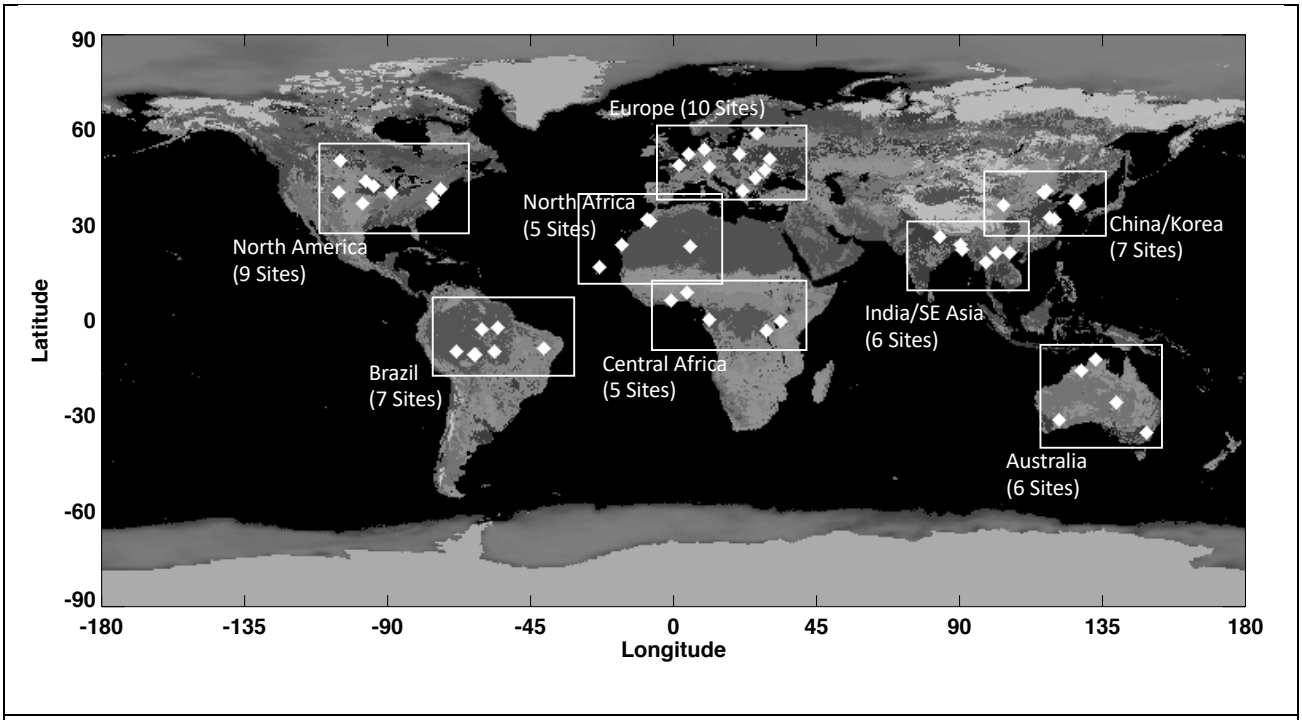

Figure 7. Location of AERONET sites and how they grouped for calculations of mean/bias/RMS with respect to MATCH and MERRA-2 optical depths found in tables 3 and 4.

MATCH AOD for the Brazil group is biased high by 0.02, and the China/Korea group has no appreciable bias compared with AERONET AODs. These two regions have relatively large bias of $\langle AOD_{MODIS}^{clr} \rangle$ from MATCH compared with MODIS AODs (**Fig. 3** right). In contrast, negative bias of MERRA2 AODs compared with AERONET AODs for Brazil, central Africa, and China/Korea groups are consistent with negative bias of MERRA2 $\langle AOD_{MODIS}^{clr} \rangle$ compared with MODIS AODs (**Fig. 3** left). For the China/Korea group, the RMS difference between MATCH AODs and AERONET AODs is 0.18 and correlation coefficient is 0.7. These are worse than the counterpart values of MERRA2 versus AERONET AODs because summertime agreement between MATCH and AERONET AODs is worse if a similar plot as **Fig. 6** is plotted for summertime when hygroscopic aerosols are dominant under high relative humidity conditions.

The sign of the MATCH AODs compared to AERONET AODs for all-sky conditions is generally consistent with the sign of clear-sky counterparts. The RMS difference under all-sky conditions is generally larger than the clear-sky RMS difference while the correlation coefficient is nearly the same. The biases for MERRA2 comparisons are generally comparable to MATCH though RMS for MERRA2 tend to be slightly smaller and correlations tend to be higher due in part to the assimilation of AERONET into the MERRA2 model.

Table 3. Hourly AERONET station statistics for MATCH and MERRA-2.
Continental Groups, Clear Sky conditions[1]

				MATCH			MERRA-2		
Site	Predominant Aerosol Type	Number	Observed Average	Bias	RMS	R^2	Bias	RMS	R^2
Australia (5 Sites)	Dust Smoke	20925	0.06	0.01	0.06	0.4	0.03	0.05	0.7
Brazil (7 Sites)	Smoke Polluted	6554	0.14	0.02	0.10	0.8	-0.02	0.08	0.9
Central Africa (5 Sites)	Smoke	2139	0.70	-0.10	0.24	0.9	-0.10	0.24	0.9
North Africa (5 Sites)	Dust	10047	0.17	0.07	0.15	0.7	0.02	0.10	0.8
China/Korea (8 Sites)	Polluted	2827	0.26	-0.00	0.18	0.7	-0.03	0.15	0.8
India/SE Asia (6 Sites)	Smoke Polluted	3010	0.51	-0.09	0.28	0.6	-0.10	0.24	0.8
North America (9 SIte)	Continental Polluted	21429	0.10	-0.00	0.07	0.7	0.00	0.06	0.8
Europe (10 Sites)	Continental Polluted	10211	0.13	0.01	0.07	0.7	-0.02	0.05	0.8

[1]The time period used is from Mar 2000 through Apr 2020. Actual period varies by site depending on AERONET data availability. Clear Sky is identified by MODIS and geostationary satellites and the cloud fraction is less than 1% over a SYN1deg grid box.

359

Table 4. Hourly AERONET station statistics for MATCH and MERRA-2.
Continental Groups, All Sky Conditions[1]

				MATCH			MERRA-2		
Site	Predominant Aerosol Type	Number	Observed Average	Bias	RMS	R^2	Bias	RMS	R^2
Australia (5 Sites)	Dust Smoke	110523	0.09	0.00	0.09	0.5	0.02	0.07	0.8
Brazil (7 Sites)	Smoke Polluted	72656	0.25	0.03	0.23	0.8	-0.04	0.18	0.9
Central Africa (5 Sites)	Smoke	41193	0.55	-0.07	0.26	0.8	-0.10	0.26	0.9
North Africa (5 Sites)	Dust	43205	0.23	0.08	0.20	0.7	0.01	0.14	0.8
China/Korea (8 Sites)	Polluted	52287	0.45	0.01	0.31	0.7	-0.08	0.27	0.8
India/SE Asia (6 Sites)	Smoke Polluted	44534	0.61	-0.06	0.32	0.6	-0.10	0.32	0.7
North America (9 Sites)	Continental Polluted	160356	0.13	0.02	0.13	0.6	0.00	0.09	0.7
Europe (10 Sites)	Continental Polluted	175010	0.18	0.04	0.14	0.6	-0.02	0.08	0.8

[1] The time period used for the statistics is from March 2000 through April 2020. The actual period varies by site depending on AERONET data availability.

[2] Correlation coefficient.

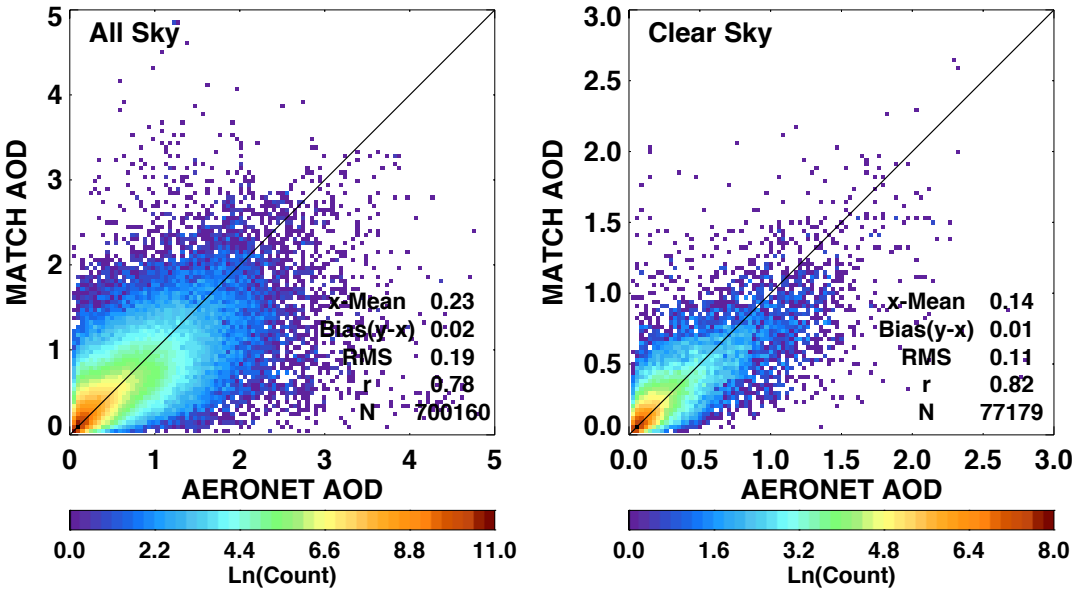

Figure 8. All sky (left) and clear sky (right) comparisons of observed (AERONET) hour mean optical depths to estimates from the MATCH model for 20+ years at 55 AERONET sites shown in **Fig 7**.

Results for all points across all sites and times are shown in **Figure 8**. The color density plots are in log scale and indicate the vast majority of observations have an AOD of less than one for both clear and all sky conditions observed within the SYN1deg grid box. Biases are less than 10% of the mean value but RMS is large relative to the mean observed value. Overall correlation is approximately 0.8. The 'clear sky' hours (where SYN1deg estimated less than 1% cloud in the grid box based on MODIS and GEO observations) is a little more than 10% of the overall points. When MATCH AOD is compared to MERRA2 AOD (not shown) MATCH is biased approximately 10% higher.

3. Discussion of AOD Differences

In this section, we investigate the reason for the AOD differences shown in the previous section. In addition, we estimate the effect of the AOD differences to surface irradiances when MATCH AODs are used for surface irradiance computations.

Generally, cloud contamination in MODIS AODs is caused by unresolved sub-pixel scale clouds (Kaufman et al. 2005; Martins et al. 2002). The difference shown over convective regions, therefore, seems to be caused by the uncertainty due to 3D radiative effects that impact retrieved AODs by unknown amounts (Wen et al. 2007), by errors in estimating the fraction of hygroscopic aerosols or by the errors in estimating water uptake by hygroscopic aerosols (Su et al 2008). Larger AODs are screened out in the MOD08 data product while the CERES team uses all retrieved AODs regardless of the QAC score. The comparison with AERONET AODs is not decisive to determine how to screen MODIS AODs because MATCH AODs are positively biased and MERRA2 AODs are negatively biased for the Brazil group. The result underscores the difficulty of deriving accurate AODs, which appear to involve requirements in addition to identification of clear-sky scenes. Levy et al. (2013) list reasons lowering the QAC score as 1) pixels are thrown out due to cloud masking, 2) retrieval solution does not fit the observation well, and 3) the solution is not physically plausible given the observed situation. Therefore, even though the difficulty of identifying clear-sky scenes is driven by cloud contamination by trade cumulus (Loeb et al. 2018), the difficulty of deriving AODs exists over convective regions (Varnai et al., 2017).

Larger positive biases of MATCH AODs compared with AERONET AODs exist over Africa (Tables 3 and 4). For North Africa, the bias is known to be caused by

excessive dust generated by the MATCH algorithm. Even though modeled aerosols are not often used over north Africa owing to the abundance of clear-sky conditions, the dust problem leads to a larger positive AOD bias. In addition, MATCH uses fixed aerosol sources in time. Therefore, it tends to miss large aerosol events, such as forest fires, until clear-sky conditions occur, allowing observations of the event by MODIS. This leads to a larger RMS difference and lower correlation coefficient with AERONET AODs compared with those from MERRA2 versus AERONET.

Because MODIS AOD are not generally available under overcast conditions, the reliance on modeled AOD increases as the cloud fraction over a 1°×1° grid increases. **Figure 6**, which shows that AERONET AOD increases with cloud fraction derived from satellites, indicates that as the cloud fraction over a 1°×1° grid increases, AOD over the clear-sky portion of the grid increases. In addition, **Fig. 6** suggests that modeled AODs under near overcast conditions are significantly larger than clear-sky AODs that are constrained by MODIS observations. Because we are not able to evaluate AODs under overcast conditions, here we only assess AOD changes with cloud fraction using ground-based observations. **Figure 9** shows the distribution of AERONET AODs for clear-sky and all-sky conditions, as well as precipitable water derived from a microwave radiometer separated by these two conditions. Clear-sky is identified by the Long-Ackerman algorithm (Long et al. 2006) that uses surface direct and diffuse irradiances. **Figure 9** shows that AOD and precipitable water under all-sky conditions are significantly larger than those under clear-sky conditions. When we use cloud fraction derived from satellite and plot AOD and precipitable water as a function of the cloud fraction using the same grid box where the ground site is located, AOD and precipitable

water increase with the cloud fraction (**Fig. 10**). Therefore, increasing AOD with cloud fraction shown in **Fig. 6** is qualitatively explained by increasing AOD of hygroscopic aerosols with relative humidity. However, **Fig. 10** indicates that either the growth of MATCH AOD is too strong or modeled MATCH AOD under all-sky conditions is too large.

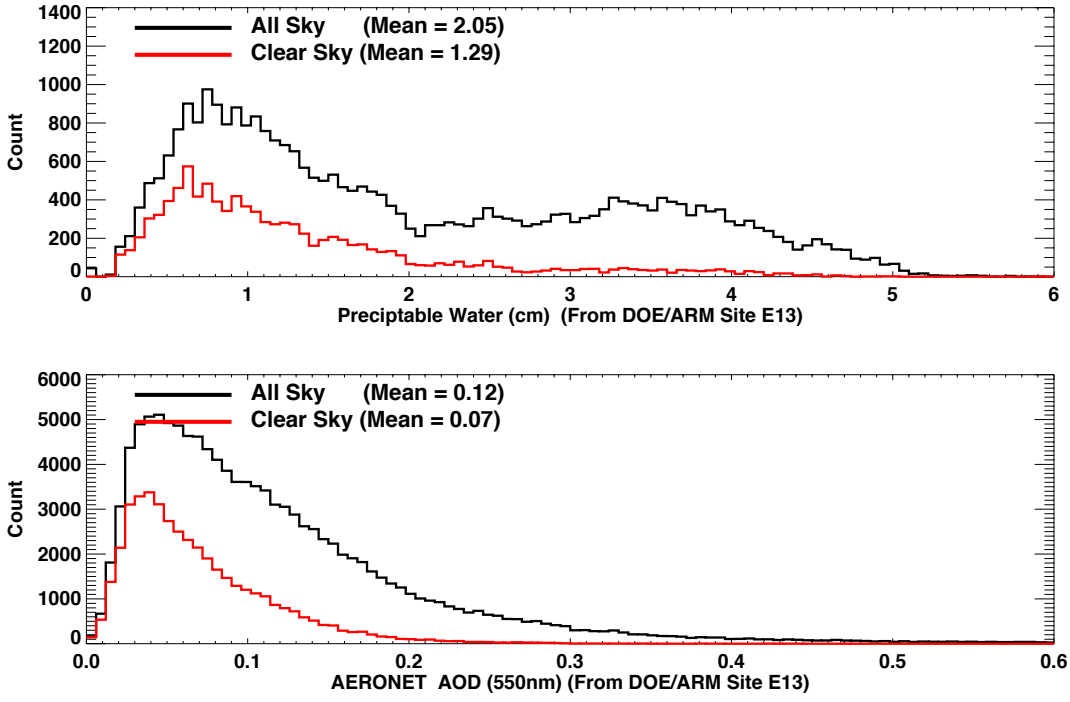

Figure 9. a) 15-minute mean precipitable water distributions from Microwave radiometer observations at ARM/SGP E13 site under all sky and clear sky conditions. b) 15-minute mean aerosol optical depth distributions from AERONET sun-photometer at 550nm. 'Clear sky' is here defined as when a 15-minute time period where the SWFA, surface radiometry-based cloud fraction, equals 0.

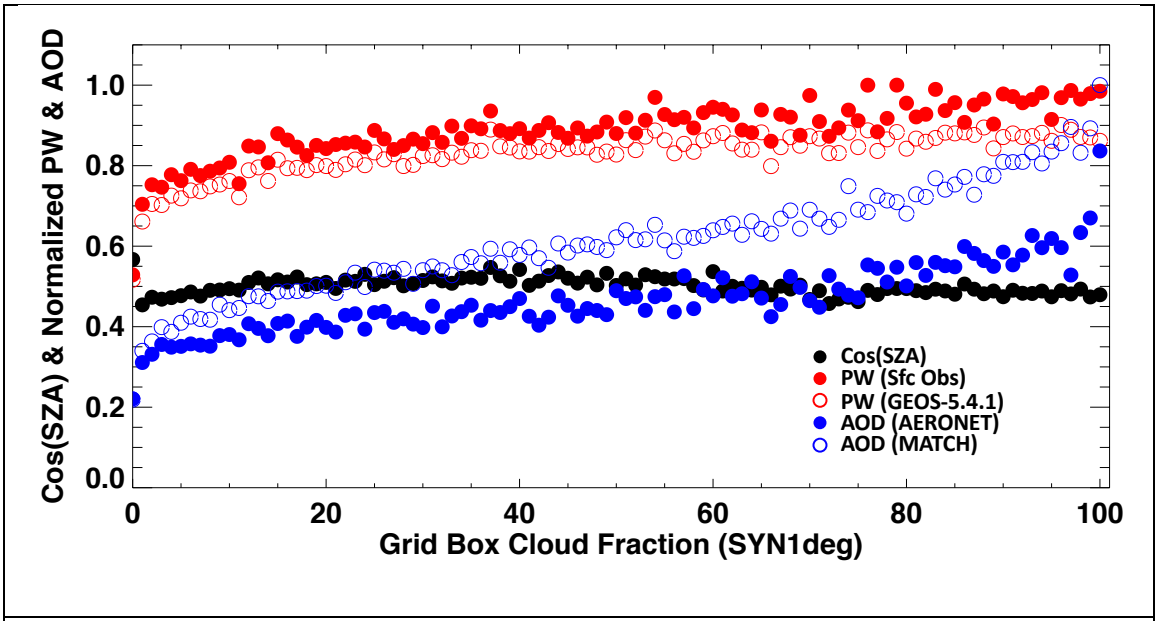

Figure 10. Aerosol optical depth (AOD) and precipitable water (PW) as a function of cloud fraction over the 1°×1° grid box where the ARM/SGP E13 and SURFRAD Bondville IL sites are located. Closed and open blue circles are, respectively, AOD derived from AERONET and MATCH AOD. Closed and open red circles are, respectively, PW derived from microwave radiometer and CIMEL sun photometer and GEOS-5.4.1 PW. Cloud fractions are derived from MODIS and geostationary satellites. Black dots are mean cosine solar zenith angle of the time of AOD and PW observations. AOD and PW are normalized to their maximum value for display.

429

430

431

432

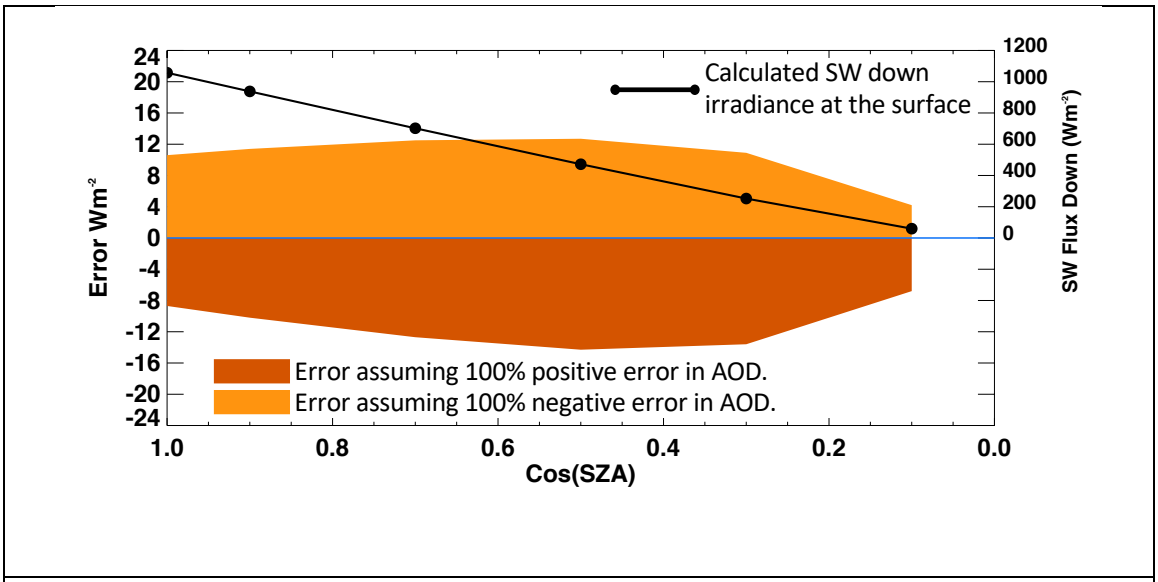

Figure 11. Estimated downward SW flux at the surface from the Langley Fu & Liou model along with estimated error in surface SW down +/-based on 100% error in AOD as a function of cos(SZA).

433

434

435 **3.1 Effect of AOD differences on surface irradiances**

436 **Figure 11** shows a summary of a series of radiative transfer calculations using the

437 "On-Line Langley Fu & Liou radiative transfer code:

438 https:// cloudsgate2.larc.nasa.gov/cgi-bin/fuliou/runfl.cgi

439 with an open shrub spectral albedo (broadband albedo of 0.14 at μ_0=1.0), "continental"

440 aerosol, and no clouds. Values on the solid black line are the calculated surface

441 downward irradiances with an AOD of 0.09 at six different solar zenith angles.

442 Calculations were then done for AOD's of 0.0 and 0.18, at the same solar zenith angles,

443 representing 100% error bounds of the mean AODs derived from AERONET (as seen in

444 Tables 3 and 4 for the Australia sites where the RMS is approximately equal to the

445 observed average of AOD). The orange and red shaded areas indicate potential bias of

446 the downward shortwave irradiance at a given solar zenith angle. Irradiance values scale

447 nearly linearly between these limits. **Figure 11** shows the error remains nearly constant
448 until a μ_0=0.5 where it begins to decrease as insolation decreases. However, due to longer
449 path lengths at large solar zenith angles, the percentage error actually increases.
450
451 **4. Clear Sky Comparisons of SYN1deg and Surface Observed Irradiances**
452 We complete our analysis of the impact of the MATCH aerosols on computed
453 surface irradiances by comparing calculated hourly mean surface downward shortwave
454 irradiance from the Ed4.1 SYN1deg-Hour product to observations of downward
455 shortwave irradiances. In a 1°×1° grid box with an approximate size of 111 km ×111 km,
456 100% clear sky sampled over one hour as determined by MODIS or geostationary
457 satellites is relatively rare. None the less, by grouping sites based on general surface
458 conditions and analyzing 20 years of data sufficient samples are found. **Figure 12** shows
459 the sites as grouped by color including 15 land sites labeled "Mid-Latitude" (Green
460 triangles), 6 sites labeled "Desert" (Red), 6 sites labeled "Polar" (White) and 46 buoys
461 (Blue). Surface observed SW irradiance from the land sites comes from the Baseline
462 Surface Radiation Network (Ohmura et al. 1998; Dreimel et al. 2018) and buoy data are
463 made available

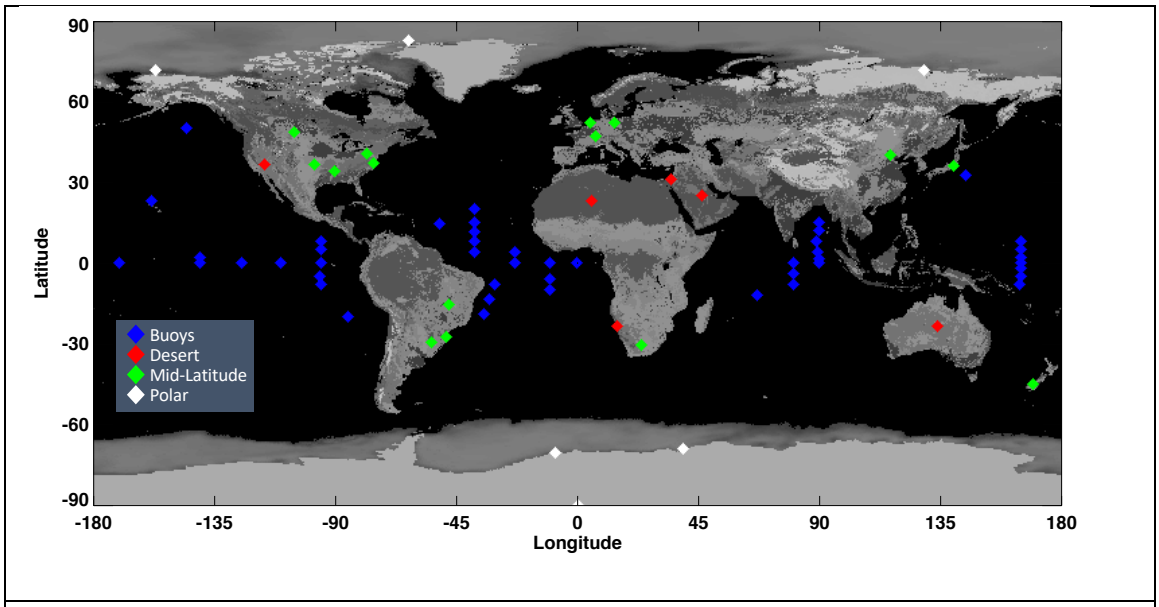

Figure 12. Location of surface observations of downwelling shortwave irradiance used to compare the SYN1deg Ed4.1 calculations to observations for all available hours (from Mar 2000 through Dec 2019) where the SYN1deg cloud analysis determines the hour to be 100% clear sky.

from the Pacific Marine Environmental Lab (PMEL) (McPhaden et al. 2002, 2009) and the Woods Hole Oceanographic Institute (WHOI) (Colbo and Weller, 2009). A complete listing is given in Appendix A.

Figure 13 shows hourly comparisons of computed clear-sky downward shortwave irradiance compared to observations for the four groups of sites shown in **Fig. 12**. In general, the calculated irradiance is larger than observed downward shortwave irradiance. There we find that in every grouping, SYN1deg calculations tend to be too transmissive, overestimating the surface downwelling SW irradiance by between 4 Wm^{-2} (polar sites) and 16 Wm^{-2} (ocean buoys) with mid-latitude and desert sites each overestimating DSF by ~10 Wm^{-2}. It's notable that the smallest overestimation is in polar regions where column AOD would be the smallest. This points to the possibility that MATCH is weighted too far towards scattering aerosols and too few absorbing aerosols.

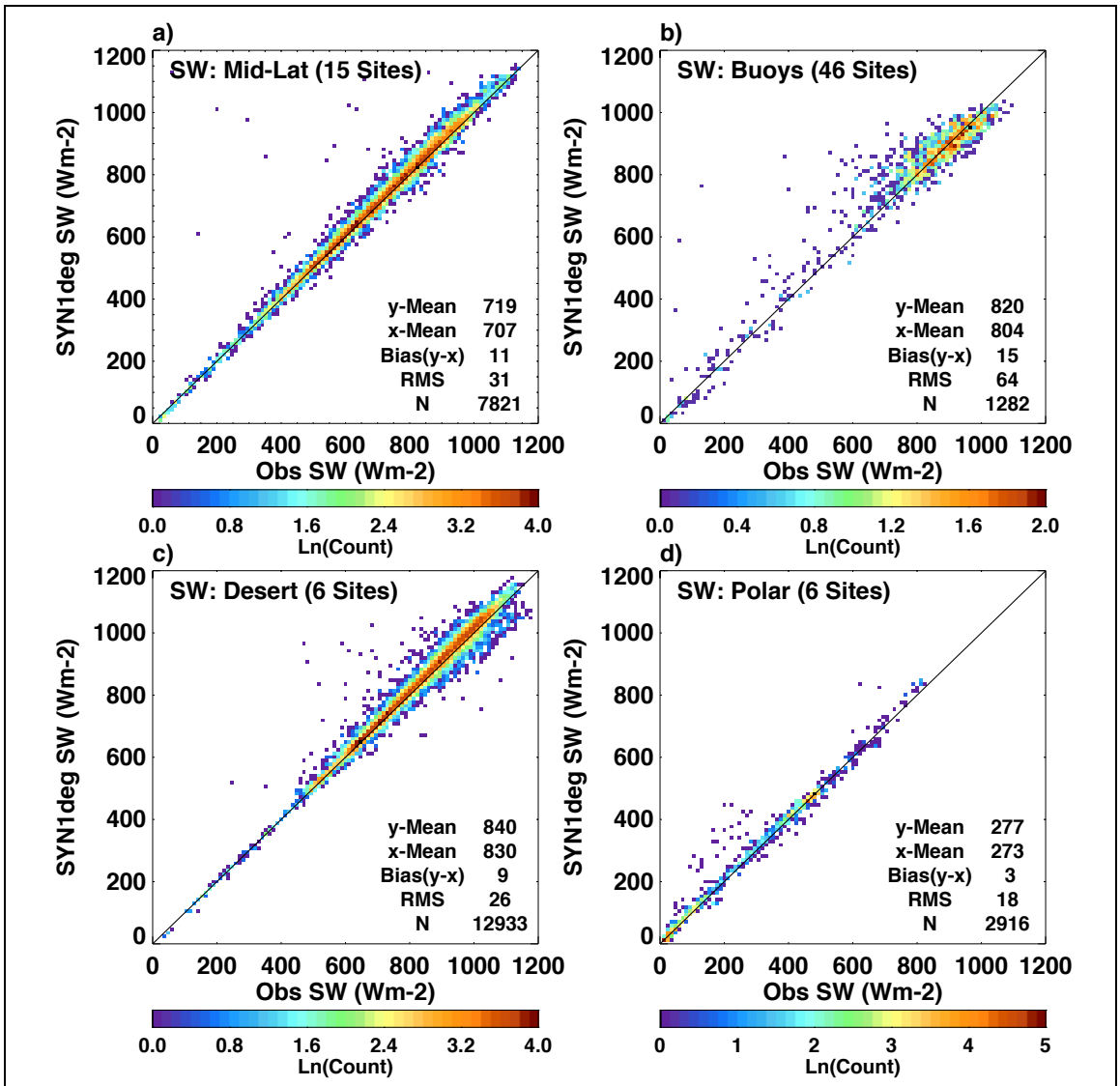

Figure 13. Comparisons of SW downward irradiance at the surface from the SYN1deg Ed4.1 calculations (y-axis for all plots) and BSRN and buoy surface sites (x-axis all plots). Data are from Mar 2000 through Feb 2020 and only include hours when a 1x1 grid box is 100% clear sky according to SYN1deg cloud fraction.

Clear-sky scenes used for **Fig. 13** are those identified by MODIS and geostationary satellites over the 1°×1° grid where the ground site is located. That is, when the satellites did not detect clouds over the one-hour period within the grid box, we compared the computed and observed hourly mean downward shortwave irradiances. Downward SW irradiance is nominally measured by a shaded pyranometer combined

483 with the direct insolation measured by a pyrheliometer on a solar tracker. Though the
484 satellite may indicate clear, clouds might have been present within the field-of-view of
485 the pyranometer increasing diffuse radiation. This would increase the observed
486 downward shortwave irradiance, hence the modeled irradiance would be smaller. To
487 verify, we used the ground-based cloud screening algorithm developed by Long and
488 Ackerman (Long et al. 2006) to further screen clouds. For the land groupings, plots
489 showing the difference between calculation minus observation as a function of
490 observation, utilizing both the satellite and surface based observed cloud fraction to 0.0,
491 are shown in **Fig. 14**. As shown in the plot, mean bias did not change significantly.
492 However, the RMS in both the Mid-Latitude and Desert sites was reduced by half due to
493 the more stringent cloud screening (**Fig. 14**).
494

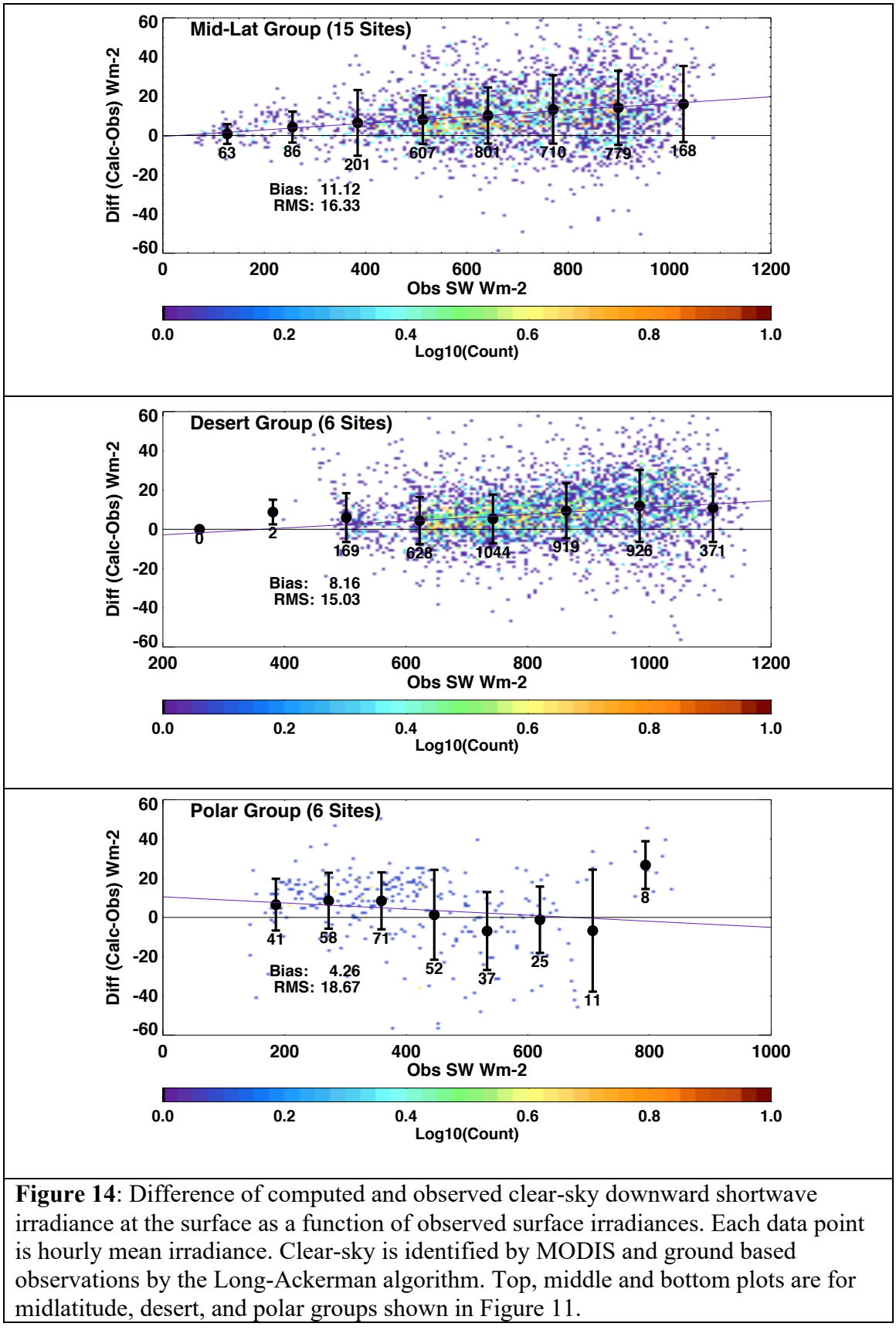

Figure 14: Difference of computed and observed clear-sky downward shortwave irradiance at the surface as a function of observed surface irradiances. Each data point is hourly mean irradiance. Clear-sky is identified by MODIS and ground based observations by the Long-Ackerman algorithm. Top, middle and bottom plots are for midlatitude, desert, and polar groups shown in Figure 11.

CERES instruments observe TOA irradiances, which can be used to assess the bias in computed irradiance. Global annual mean clear-sky TOA irradiances derived from CERES observation averaged over 20 years from March 2000 through February 2020 are 53 Wm-2 for reflected shortwave irradiance and 268 Wm-2 for emitted longwave irradiance. Corresponding computed reflected shortwave flux is 51 Wm-2 and emitted longwave flux is 267 Wm-2. Insight into the surface irradiance errors may be gained by considering how surface irradiance is modified via the tuning algorithm to match TOA irradiance in the CERES EBAF-surface product (Kato et al. 2018). After known biases are taken out, the adjustment of temperature and specific humidity profiles, surface and aerosol properties are derived based on their pre-assigned uncertainty and the difference of computed and observed TOA shortwave and longwave irradiance using the Lagrange multiplier approach. To match the computed shortwave and longwave fluxes, AOD is increased from 0.136 to 0.156 (global annual mean values) and precipitable water is decreased from 2.29 cm to 2.22 cm (global annual mean values). These adjustments change the downward shortwave irradiance from 244 Wm-2 to 243 Wm-2.

To analyze how the EBAF tuning process changes surface irradiance, AOD and precipitable water, we computed the mean change separated by surface group shown in Fig 13. Generally, AOD increases and precipitable water decreases to increase reflected shortwave flux, which in turn decreases surface downward shortwave irradiance over these regions (**Table 5**). For the midlatitude group, on average, AOD is increased by 0.02, precipitable water is decreased by 0.06 cm, and surface albedo is increased by 0.03. These adjustments reduce the diurnally averaged downward shortwave irradiance at the surface by 2 Wm^{-2}. We do not have exact matches of BSRN and AERONET surface sites

518 but Tables 3 and 4 show MATCH AODs have either no bias (north America and China
519 and southeast Asia) or slightly negatively biased by 0.01 (Europe). Therefore, increasing
520 MATCH AODs by 0.02 on average for the mid-latitude group seems justifiable.
521 However, decreasing 2 Wm^{-2} for the diurnally averaged downward shortwave is smaller
522 than the 12 Wm^{-2} bias shown in the top right plot of **Fig. 11**, although instantaneous
523 irradiances are used for **Fig. 10**. The positive bias found in the downward shortwave
524 irradiance for the North Africa group (Fig 12c) is not consistent with the positive bias of
525 aerosol optical depth shown in Table 3 under clear-sky conditions.
526 The adjustment made to match TOA shortwave irradiance, in the EBAF product,
527 is within the uncertainty of MODIS-derived AOD of ±0.05 over land and ±0.03 over
528 ocean (Remer et al. 2008; Levy et al. 2010, 2013). However, these are an expected error
529 of instantaneous AOD retrieval derived from the comparison of AODs with AERONET.
530 Therefore, the bias averaged over ground sites and many years is expected to be much
531 smaller. Although, the 0.03 AOD adjustment over ocean might be the upper limit of the
532 uncertainty of MODIS AODs over ocean, 16 Wm^{-2} bias in the instantaneous downward
533 shortwave irradiance seems to be larger than the reduction by 2 Wm^{-2} in the diurnally
534 averaged downward shortwave irradiance.
535 While we cannot identify the cause of the discrepancy between AOD comparison
536 and downward shortwave irradiance comparison with surface observations, potential
537 issues are following. 1) Aerosol type and optical properties used in irradiance
538 computations, and 2) bias in downward shortwave irradiance measured by pyranometer,
539 especially diffuse irradiance at smaller solar zenith angles. Because of the temperature
540 gradient within pyranometer, the downward shortwave irradiance measured by a

pyranometer tends to be biased low under clear-sky condition (Haeffelin et al. 2001). Note that a study by Ham et al. (2020) indicates that the bias of diurnally averaged surface downward shortwave irradiance computed by a four-stream model should be smaller than 1%.

Table 5: Radiative flux, aerosol optical depth (AOD), precipitable water, and surface albedo change to match observed top-of-atmosphere radiative fluxes

		Changes: adjusted - unadjusted				
	Observed TOA upward shortwave irradiance (Wm^{-2})	Clear-sky TOA upward shortwave irradiance (Wm^{-2})	Clear-sky surface downward shortwave irradiance (Wm^{-2})	Clear-sky AOD	Clear-sky precipitable water (cm)	Clear-sky surface albedo
Mid-latitude	63.3	3.9	-2.0	0.02	-0.06	0.03
Desert	92.3	3.4	-1.7	0.02	-0.04	0.01
Polar	86.5	8.2	-0.2	0.01	-0.03	0.10
Buoys	42.0	1.6	-2.0	0.03	-0.12	0.00

5. Conclusions

We evaluated MATCH aerosol optical depth used to produce the CERES SYN1deg product. Aerosol optical depths derived from Terra and Aqua by the dark target and deep blue algorithms were merged to produce daily gridded AODs. Daily gridded AODs were used for assimilation by MATCH at local solar noon. As a consequence, monthly mean AODs under clear-sky conditions identified by MODIS closely agree with those derived from MODIS, although MATCH uses climatological aerosol sources. Because AODs are not screened by QAC, MATCH AODs are larger over convective regions (e.g. Amazon, central Africa, and south east Asia) for both clear-sky and all-sky conditions.

559 MATCH AODs under all-sky conditions are larger than those under clear-sky
560 conditions. Time series of AERONET AODs indicate that AODs generally increase with
561 cloud fraction, which is consistent with, primarily, water uptake by hygroscopic aerosols
562 (Varnai et al, 2017). In addition, surface observations at the ARM SGP site suggest that a
563 larger AODs and larger precipitable water under all-sky conditions than those under
564 clear-sky conditions. Aerosol optical depth biases from AERONET AODs are
565 comparable to biases of MERRA2 AOD biases from AERONET AODs for both all-sky
566 and clear-sky conditions. However, MERRA2, which uses AERONET AODs to train the
567 algorithm, has better temporal correlation with AERONET AODs than MATCH AODs.
568 Once MATCH AODs are used for surface irradiance computations, downward
569 shortwave irradiances are positively biased by 1% to 2% compared to those observed at
570 surface sites. Top-of-atmosphere reflected clear-sky shortwave irradiances are negatively
571 biased compared with those derived from CERES observations. Increasing AODs by
572 ~0.02, and surface albedos by 0.03, and decreasing precipitable water by 0.06 cm over
573 mid-latitude surface sites makes computed reflected TOA irradiances agree with those
574 derived from CERES. These adjustments reduce downward shortwave irradiances at the
575 surface by 2 Wm^{-2}. Decreasing MATCH AODs for the desert group is needed to match
576 computed reflected shortwave irradiances at TOA with those derived from CERES.
577 However, decreasing MATCH AODs is not consistent with generally larger MATCH
578 AODs compared with AERONET.
579 Although optical properties of aerosols (i.e. aerosol type) play a role in computing
580 shortwave irradiance, changing aerosol type can alter the downward shortwave irradiance
581 in the right direction. We did not investigate the error in aerosol type in this study.

582 Aerosol types used in irradiance computations rely on those modeled by MATCH. Biases
583 in the fraction of each aerosol type and their optical properties can change TOA upward
584 and surface downward shortwave irradiances without altering total AOD. Evaluation of
585 aerosol type is left for the future study.
586
587 **Acknowledgments**
588 This work was funded by the NASA CERES project. The products and the
589 validation could not have been accomplished without the help of the CERES TISA team.
590 These data were obtained from the NASA Langley Research Center EOSDIS Distributed
591 Active Archive Center. We also wish to acknowledge the hard work put in by the many
592 dedicated scientists maintaining surface instrumentation in many diverse climates to
593 obtain high quality observations of downwelling shortwave and longwave surface flux.
594 Those groups are noted in Appendix A.
595
596 **Appendix A. Surface Observation Sites Used for Validation**
597 A great deal of data used in this study was collected by dedicated site scientists
598 measuring critical climate variables around the world. The tables included in this
599 appendix outline the sites, in situ measurements taken and their locations and dates of
600 available data. Table A1 lists the locations of the AERONET sites, our source for
601 observed aerosol optical depth which can be found on-line at:
602 https://aeronet.gsfc.nasa.gov/new_web/index.html.
603
604

Table A1. AERONET Observation Sites

Region	Site	Location	Available Months
North Africa (6 Sites)	Saada, Morocco	31.6N, 8.2W	2004/07 - 2019/04
	Ouarzazate, Morocco	30.9N, 6.9W	2012/02 - 2015/06
	Tenerife Isl., Spain	28.3N, 16.5W	2004/07 - 2019/04
	Dhaka, Morocco	23.7N, 15.9W	2002/02 - 2005/11
	Tamanrasset, Algeria	22.8N, 8.2E	2004/07 - 2019/04
	Cape Verde Island	16.7N, 22.9W	2000/03 - 2018/12
Central Africa (5 Sites)	Ilorin, Nigeria	8.5N, 4.7E	2000/03 - 2019/09
	Koforidua, Ghana	6.1N, 0.3W	2012/12 - 2019/04
	Lope, Gabon	0.2S, 11.6E	2014/04 - 2018/02
	Mbita, Kenya	0.4S, 34.2E	2006/03 - 2017/17
	Bujumbura, Burundi	3.4S, 29.4E	2013/12 - 2019/04
China, Korea (8 Sites)	Xinglong, China	40.4N, 117.6E	2006/02 - 2014/11
	Beijing, China	39.9N, 116.4E	2001/03 - 2019/03
	Anymon Isl, S Korea	36.5N, 126.3E	2000/03 - 2019/11
	Yonsei Univ, S Korea	37.6N, 126.9E	2011/03 - 2019/01
	Cuiying Mt, China	35.9N, 104.1E	2006/07 - 2013/05
	Nanjing, China	32.2N, 118.7E	2008/03 - 2010/04
	Taihu, China	31.4N, 120.2E	2005/09 - 2016/08
	XiangHe, China	39.7N, 116.9E	2001/03 - 2017/05
India, SE Asia (8 Sites)	Gandhi College, India	25.8N, 84.1E	2006/04 - 2019/11
	Luang Namtha, Laos	20.9N, 101.4E	2001/04 - 2019/02
	Omkoi, Thailand	17.8N, 98.4E	2003/02 - 2018/03
	Dhaka Univ, Bangledesh	23.7N, 90.3E	2012/06 - 2019/07
	Bhola, Bangledesh	22.2N, 90.7E	2013/04 - 2019/04
	Nghia Do, Vietnam	21.0N, 105.8E	2010/11 - 2019/09
	Pune, India	18.5N, 73.8E	2004/10 - 2019/06
	Hanimaadhoo, Maldives	6.7N, 73.2E	2004/11 - 2019/09

Table A1. AERONET Observation Sites (Continued)

Region	Site	Location	Available Months
Brazil (7 Sites)	Petrolina, Brazil	9.1S, 40.4W	2004/07 - 2016/11
	Abracos Hill, Brazil	10.7S, 62.4W	2000/03 - 2005/10
	Alta Floresta, Brazil	9.9S, 56.1W	2000/05 - 2019/02
	Belterra, Brazil	2.6S, 55.0W	2000/03 - 2005/04
	Ji Parana SE, Brazil	10.9S, 61.9W	2006/01 - 2017/10
	Manaus, Brazil	2.9S, 60.0W	2011/02 - 2019/05
	Rio Branco, Brazil	9.9S, 67.9W	2000/07 - 2017/10
Australia (6 Sites)	Jabiru, Australia	12.6S, 132.9E	2000/03 - 2019/09
	Lake Argyle, Australia	16.1S, 128.7E	2001/10 - 2019/09
	Canberra, Australia	35.3S, 149.1E	2003/01 - 2017/08
	Birdsville, Australia	25.9S, 139.3E	2005/08 - 2018/06
	Lucinda, Australia	18.5S, 146.4E	2009/10 - 2020/01
	Lake Lefroy, Australia	31.2S, 121.7E	2012/06 - 2019/12
North America (10 Sites)	Brats Lake, Canada	50.2N, 104.7W	2000/03 - 2013/02
	Sioux Falls, SD	43.7N, 96.6W	2001/06 - 2017/10
	Ames, IA	42.0N, 93.8W	2004/05 - 2019/03
	Boulder Tower	40.0N, 105W	2001/05 - 2016/07
	Bondville, IL	40.0N, 88.4W	2000/03 - 2017/10
	Brookhaven, NY.	40.8N, 72.9W	2002/09 - 2020/01
	Wallops Island, VA	37.9N, 75.5W	2003/03 - 2020/03
	ARM/SGP E13	36.6N, 97.5W	2000/03 - 2018/05
	Chesapeake Light Tower	36.9N, 75.7W	2000/03 - 2016/01
	Table Mountain, CO	40.1N, 105.2W	2008/11 - 2017/12
Europe (10 Sites)	Cabauw, Netherlands	51.9N, 4.9E	2003/04 - 2017/11
	Palaiseau, France	48.7N, 2.2E	2000/03 - 2020/10
	Torevere, Estonia	58.2N, 26.5E	2002/06 - 2019/07
	Kishinev, Moldova	47.0N, 28.8E	2000/03 - 2018/11
	Belsk, Poland	51.8N, 20.8E	2004/01 - 2016/08
	Kyiv, Ukraine	50.3N, 30.5E	2007/04 - 2018/12
	Hamburg, Germany	53.5N, 9.9E	2000/06 - 2018/06
	Munich Univ, Germany	48.1N, 11.6E	2001/11 - 2019/05
	Thessaloniki, Greece	40.6N, 22.1E	2003/06 - 2020/03
	Bucharest, Hungary	44.3N, 26.0E	2000/10 - 2019/03

Sources of surface observed downwelling irradiance are outlined in Tables A2 (land) and A3 (buoys). For land we utilize data from the Baseline Surface Radiation Network (BSRN) (Dreimel et al, 2018; Ohmura et al. (1998)), the US Dept. of Energy's Atmospheric Radiation Measurement (ARM) program and NOAA's SURFRAD network available from NOAA's Air Resources Laboratory/Surface Radiation Research Branch., Augustine et al. (2000). Buoy observations come from

two sources through four separate projects. The Upper Ocean Processes group at Woods Hole Oceanographic Institute have maintained the Stratus, North Tropical Atlantic Site (NTAS) and Hawaii Ocean Time Series (HOTS) buoys for more than a decade providing valuable time series of radiation observations in climatically important regions of the ocean. These data can be retrieved from: http://uop.whoi.edu/index.html. We would also like to acknowledge the Project Office of NOAA's Pacific Marine Environmental Labs (PMEL) where three groups of buoy data were downloaded: In the Pacific, the Tropical Atmosphere Ocean/Triangle Trans-Ocean Buoy Network (TAO/TRITON) (McPhaden, 2002) data, from the tropical Atlantic Ocean, the Prediction and Research Moored Array in the Tropical Atlantic (PIRATA) (Servain et al. 1998), and the Research Moored Array for African - Asian - Australian Monsoon Analysis and Prediction (RAMA) (McPhaden et al., 2009) in the Indian Ocean. Also downloaded from PMEL are the long-term buoy observations PAPA and Kuroshio Current observatory sites.

655

656

Table A2. Surface Irradiance Validation Sites (Land)

Region	Site	Location	Source
Mid-Latitude (15 Sites)	Lindenberg, Germany	52.2N, 14.1E	BSRN
	Cabauw, Netherlands	51.9N, 4.9E	BSRN
	Fort Peck, MT	48.3N, 105.1W	BSRN
	Payerne, Switzerland	46.8N, 6.9E	BSRN
	Penn State, PA	40.7N, 77.9W	SURFRAD
	Beijing, China	39.9N, 116.3E	BSRN
	E13, Lamont, OK	36.6N, 97.5W	ARM
	Ches Light Tower, USA	36.9N, 75.7W	BSRN
	Tateno, Japan	36.1N, 140.1E	BSRN
	Goodwin Creek, MS	34.2N, 89.9W	SURFRAD
	De Aar, South Africa	30.6S, 24.0E	BSRN
	Lauder, New Zealand	45.0S, 169.7E	BSRN
	Florianapolis, Brazil	27.5S, 48.5W	BSRN
	Brasilia, Brazil	15.6S, 47.7W	BSRN
	Sao Martinho da Serra, Brazil	29.4S, 53.8W	BSRN
Desert (6 Sites)	Sede Boqer, Israel	30.8N, 34.7E	BSRN
	Saudi Solar Village	24.9N, 46.4E	BSRN
	Tamanrasset, Algeria	22.8N, 5.5E	BSRN
	Desert Rock, NV	36.6N, 116.1W	SURFRAD
	Alice Springs, Australia	23.7S, 133.8E	BSRN
	Gobabeb, Namibia	23.5S, 15.0E	BSRN
Polar (6 Sites)	Alert,Canada	82.5N, 62.4W	BSRN
	Tiksi, Russia	71.6N, 128.9E	BSRN
	Barrow, Alaska	71.3N, 156.7W	BSRN
	Syowa, Antarctica	69.0S, 39.5E	BSRN
	South Pole, Antarctica	90.0S, 0.5E	BSRN
	G. von Neumayer, Antarctica	-70.6S, 8.3W	BSRN

657 BSRN: Baseline Surface Radiation Network, http://bsrn.awi.de/
658 SURFRAD: NOAA- SURFace RADiation Program, http://www.esrl.noaa.gov/gmd/grad/surfrad/
659 ARM: US Dept of Energy, Atmospheric Radiation Measurement Program, http://www.arm.gov/
660

Table A3. Surface Observation Sites for Ocean Buoy Locations

Program Name	Data Source	Locations
Upper Ocean Processes Group (UOP) 3 Buoys	Woods Hole Oceanographic Institute	Stratus Buoy -20.2N, 85.0W
		North Tropical Atlantic Buoy 14.5N, 51.0W
		Hawaii Ocean Time Series Buoy 22.5N, 158W
PIRATA Buoys 14 Buoys	Pacific Marine Environmental Laboratory (PMEL)	East Atlantic Ocean
RAMA Buoys 10 Buoys	PMEL	Tropical Indian Ocean
TAO Array Buoys 17 Buoys	PMEL	E & W Tropical Pacific Ocean
Kuroshio Extension Observatory Buoy	PMEL	NW Pacific, 32.4N, 144.6E
PAPA Sub-Arctic Ocean Buoy	PMEL	NE Pacific, 50.1N, 144.8W

661 UOP: http://uop.whoi.edu/projects/projects.htm
662 PMEL: http://www.pmel.noaa.gov/tao/data_deliv/deliv.html

663

664

665 **References**

666 Augustine, J. A., DeLuisi, J. J., and Long, C. N.: SURFRAD – A national surface radiation
667 budget network for atmospheric research, Bull. of Amer. Met. Soc. 81, No. 10, pp.
668 2341-2358, 2000.
669 Barth, M. C., Rasch, P. J., Kiehl, J. T., Benkovitz, C. M., and Schwartz, S. E.: Sulfur
670 chemistry in the NCAR CCM: Description, evaluation, features and sensitivity to
671 aqueous chemistry, J. Geophys. Res., 106, 20 311–20 322, 2000.
672 Bauer, S. E. and Menon, S.: Aerosol direct, indirect, semidirect, and surface albedo
673 effects from sector contributions based on the IPCC AR5 emissions for
674 preindustrial and present-day conditions, J. Geophys. Res., 117, D01206,
675 doi:10.1029/2011JD016816, 2012.
676 Benkovitz, C. M., Scholtz, M. T., Pacyna, J., Tarrason, L., Dignon, J., Voldner, E. C., Spiro,
677 P. A., Logan, J. A., and Graedel, T. E.: Global gridded inventories of anthropogenic
678 emissions of sulfur and nitrogen, J. Geophys. Res.: Atmos. 101 (D22), 29,239–
679 29,253, 1996.
680 Blanchard, D. C. and Woodcock, A. H.: The production, concentration and vertical
681 distribution of the sea-salt aerosol, Ann. Of the NY Acad. Of Sci.,
682 doi:10.1111/j.1749-6632.1980.tb17130, 1980.
683 Boucher, O., Randall, D., Artaxo, P., Bretherton, C., Feingold, G., Forster, P., Kerminen,
684 V.-M., Kondo, Y., Liao, H., Lohmann, U., Rasch, P., Satheesh, S.K., Sherwood, S.,
685 Stevens, B. and Zhang, X. Y.: Clouds and Aerosols. In: Climate Change 2013: The

686 Physical Science Basis. Contribution of Working Group I to the Fifth Assessment
687 Report of the Intergovernmental Panel on Climate Change [Stocker, T.F., D. Qin,
688 G.-K. Plattner, M. Tignor, S.K. Allen, J. Boschung, A. Nauels, Y. Xia, V. Bex and P.M.
689 Midgley (eds.)]. Chapter 7. Cambridge University Press, Cambridge, United
690 Kingdom and New York, NY, U, 2013.
691 Colbo, K. and Weller, R. A.: Accuracy of the IMET sensor package in the subtropics. J.
692 Atmos. Oceanic Technol., 26, 1867–1890,
693 https://doi.org/10.1175/2009JTECHO667.1, 2009.
694 Collins, W. D., Rasch, P. J., Eaton, B. E., B. Khattatov, V., Lamarque, J-F. and Zender, C.
695 S.: Simulating aerosols using a chemical transport model with assimilation of
696 satellite aerosol retrievals: Methodology for INDOEX. J. Geophys. Res., 106 (D7),
697 7313–7336, 2001.
698 d' Almeida, G. A., P. Koepke and E. P. Shettle: Atmospheric Aerosols: Global
699 Climatology and Radiative Characteristics. A. Deepak Publishing, 561 pp. 1991
700 Driemel, A., and Co-authors: Baseline Surface Radiation Network (BSRN): structure and
701 data description (1992–2017), Earth Syst. Sci. Data, 10, 1491-1501,
702 doi:10.5194/essd-10-1491-2018. 2018
703 Emmons, L. K., and co-authors: Description and evaluation of the Model for Ozone and
704 Related chemical Tracers, version 4 (MOZART-4), Geosci. Model Dev., **3**, 43–67.
705 www.geosci-model-dev.net/3/43/2010/, 2010.
706 Fu, Q. and Liou, K-N.: Parameterization of the radiative properties of cirrus clouds, J.
707 Atmos. Sci., 50, 2008–2025, 1993.

708 Fu, Q., Lesins, G., Higgins, J., Charlock, T., Chylek, P. and Michalsky, J.: Broadband
709 water vapor absorption of solar radiation tested using ARM data. Geophys. Res. Let.,
710 25, 1169–1172, 1998.
711 Ginoux, P., Chin, M., Tegen, I., Prospero, J. M., Holben, B., Dubovik, O. and Lin, S-J.:
712 Sources and distributions of dust aerosols simulated with the GOCART model J. of
713 Geophys. Res.: Atmos., 106, 20255-20273, doi.org/10.1029/2000JD000053, 2001.
714 Haeffelin, M., Kato, S., Smith, A. M., Rutledge, C. K., Charlock T. P. and Mahan, J. R.:
715 Determination of the thermal offset of the Eppley precision spectral pyranometer,
716 Appl. Opt. 40, 472-484, 2001.
717 Ham, S., Kato, S. and Rose, F. G.: Examining biases in diurnally-integrated shortwave
718 irradiances due to two- and four-stream approximations in cloudy atmosphere. J.
719 Atmos. Sci., 77(2), 551–581. doi: 10.1175/JAS-D-19-0215.1, 2020.
720 Hess, M., Koepke, P. and Schult, I.: Optical Properties of Aerosols and Clouds: The
721 software package OPAC. Bull. Amer. Meteor. Soc., 79, 831-844.
722 https://doi.org/10.1175/1520-0477(1998)079<0831:OPOAAC>2.0.CO;2,1998.
723 Holben B.N., Eck, T. F., Slutsker, I., Tanre, D., Buis, J. P., Setzer, A., Vermote, E.,
724 Reagan, J. A., Kaufman, Y., Nakajima, T., Lavenu, F., Jankowiak, I. and Smirnov,
725 A.: AERONET - A federated instrument network and data archive for aerosol
726 characterization, Rem. Sens. Environ., 66, 1-16, 1998
727 Hsu, N. C., Tsay, S-C, King, M. D. and Herman, J. R.: Deep Blue Retrievals of Asian
728 Aerosol Properties During ACE-Asia, IEEE Trans. On Geosci. and Rem. Sens.,
729 44(11), 2006.

730 Huneeus, N., and co-authors: Global dust model intercomparison in AeroCom phase I,
731 Atmos. Chem. Phys., 11, 7781–7816. www.atmos-chem-phys.net/11/7781/2011/
732 doi:10.5194/acp-11-7781-2011, 2011.
733 Kato, S., Loeb, N. G., Rose, F. G., Doelling, D. R., Rutan, D. A., Caldwell, T. E., Yu L.
734 and Weller, R. A.: Surface irradiances consistent with CERES-derived top-of-
735 atmosphere shortwave and longwave irradiances. J. of Clim Dyn. doi: 10.1175/JCLI-
736 D-12-00436, 2013.
737 Kato, S., Rose, F. G., Rutan, D. A., Thorsen, T. J., Loeb, N. G., Doelling, D. R., Huang,
738 X., Smith, W. L., Su, W. and Ham, S-H.: Surface Irradiances of Edition 4.0 Clouds
739 and the Earth's Radiant Energy System (CERES) Energy Balanced and Filled
740 (EBAF) Data Product. J. of Clim Dyn. doi: 10.1175/JCLI-D-17-0523.1, 2018.
741 Kaufman, Y. and co-authors: A critical examination of the residual cloud contamination
742 and diurnal sampling effects on MODIS estimates of aerosol over ocean, IEEE Trans.
743 Geosci. Rem. Sens. 43, DOI: 10.1109/TGRS.2005.858430, 2005.
744 Kinne, S. and co-authors: An AeroCom initial assessment – optical properties in aerosol
745 component modules of global models. Atmos. Chem. Phys., 6, 1815–1834.
746 www.atmos-chem-phys.net/6/1815/2006/, 2006.
747 Koch, D., and co-authors: Evaluation of black carbon estimations in global aerosol
748 models. Atmos. Chem. Phys., 9, 9001–9026. www.atmos-chem-
749 phys.net/9/9001/2009/, 2009.
750 L'Ecuyer T. S., Beaudoing, H. K., Rodell, M., Olson, W., Lin, B., Kato, S., Clayson, C.
751 A., Wood, E., Sheffield, J., Adler, R., Huffman, G., Bosilovich, M., Gu, G.,
752 Robertson, F., Houser, P. R., Chambers, D., Famiglietti, J. S., Fetzer, E., Liu, W. T.,

753 Gao, X., Schlosser, C. A., Clark, E., Lettenmaier, D. P. and Hilburn, K.: The
754 observed state of the energy budget in the early twenty-first century. J Clim
755 28(21):8319–8346. https://doi.org/10.1175/Jcli-D-14-00556.1, 2015.
756 Levy, R. C., Remer, L. A., Kleidman, R. G. , Mattoo, S., Ichoku, C., Kahn R. and Eck, T.
757 F.: Global evaluation of the collection 5 MODIS dark-target aerosol products over
758 land. Atmos. Chem and Phys., 10, 103999-10420. https://doi.org/10.5194/acp-10-
759 10399-2010, 2010.
760 Levy, R. C., Mattoo, S., Munchak, L. A., Remer, L. A., Sayer, A. M., Patadia, F. and
761 Hsu, N. C.: The Collection 6 MODIS aerosol products over land and ocean. Atmos.
762 Meas. Tech., 6, 2989-3034, 10.5194/amt-6-2989-2013, 2013.
763 Liousse, C., Penner, J. E., Chuang, C., Walton, J. J., Eddleman, H. and Cachier, H.: A
764 global three-dimensional model study of carbonaceous aerosols, J. Geophys. Res. A.,
765 101(D14), 19 411– 19 432, 1996.
766 Loeb, N. G., Kato, S., Loukachine, K. and Smith, N. M.: Angular Distribution Models for
767 Top-of-Atmosphere Radiative Flux Estimation from the Clouds and the Earth's
768 Radiant Energy System Instrument on the Terra Satellite. Part I: Methodology, J.
769 Atmos. Oceanic Technol, 22, 338-351, 2005.
770 Loeb, N. G. and Su, W.: Direct Aerosol Radiative Forcing Uncertainty Based on a
771 Radiative Perturbation Analysis. J. Climate, 23(19), 5288-5293. doi:
772 10.1175/2010JCLI3543.1, 2010.
773 Loeb, N. G., Doelling, D. R., Wang, H., Su, W., Nguyen, C., Corbett, J. G., Liang, L., Mitrescu,
774 C., Rose, F. G. and Kato, S.: Clouds and the Earth's Radiant Energy System (CERES)
775 Energy Balanced and Filled (EBAF) top-of-atmosphere (TOA) Edition-4.0 data

776 product. J. Climate, 31, 895–918, https://doi.org/10.1175/JCLI-D-17-0208.1,
777 2018.
778 Loeb, N. G., Rose, F. G., Kato, S., Rutan, D. A., Su, W., Wang, H., Doelling, D. R., Smith, W.
779 L. and Gettelman, A.: Toward a Consistent Definition between Satellite and Model
780 Clear-Sky Radiative Fluxes, J. Clim. DOI: 10.1175/JCLI-D-19-0381.1, 2020.
781 Long, C. N., Ackerman, T. P., Gaustad, K. L. and Cole, J. N. S.: Estimation of fractional
782 sky cover from broadband shortwave radiometer measurements, J. Geophys.
783 Res.,111, D11204, doi:10.1029/2005JD006475, 2006.
784 Martins, J. V., D. Tanre, D., Remer, L., Kaufman, Y., Mattoo, S. and Levy, R.: MODIS cloud
785 screening for remote sensing of aerosols over oceans using spatial variability,
786 Geophys. Res. Lett., 29, 1619, DOI:10.1029/2001GL013252, 2002.
787 McPhaden, M. J.: TAO/TRITON tracks Pacific Ocean warming in early 2002. CLIVAR
788 Exchanges, No. 24, International CLIVAR Project Office, Southampton, United
789 Kingdom, 7–9, 2002.
790 #——, and Coauthors: RAMA: The Research Moored Array for African–Asian–
791 Australian Monsoon Analysis and Pre- diction. Bull. Amer. Meteor. Soc., 90, 459–
792 480, doi:10.1175/ 2008BAMS2608.1, 2009.
793 Michalsky, J. J., Gueymard, C., Kiedron, P., McArthur, L. J. B., Philipona, R. and
794 Stoffel, T.: A proposed working standard for the measurement of diffuse horizontal
795 shortwave irradiance. J. of Geophys. Res. A., 112(D16),
796 https://doi.org/10.1029/2007JD008651, 2007.
797
798 Minnis, P., Sun-Mack, S., Chen, Y., Chang, F., Yost, C. R., Smith, W. L., Heck, P. W.,
799 Arduini, R. F., Bedka, S. T., Yi, Y., Hong, G., Jin, Z., Painemal, D., Palikonda, R.,

Scarino, B. R., Spangenberg, D. A., Smith, R. A., Trepte, Q. Z., Yang, P. and Xie, Y.: CERES MODIS Cloud Product Retrievals for Edition 4–Part I: Algorithm Changes. IEEE Transactions on Geoscience and Remote Sensing, 1-37. doi: 10.1109/TGRS.2020.3008866, 2020.

Ohmura A., Dutton, E., Forgan, B., Frohlich, C., Gilgen, H., Hegne, H., Heimo, A., Konig-Langlo, G., McArthur, B., Muller, G., Philipona, R., Whitlock, C., Dehne, K. and Wild, M.: Baseline Surface Radiation Network (BSRN/WCRP): New precision radiometry for climate change research. Bull. Amer. Meteor. Soc., 79, No. 10, 2115-2136, 1998.

Randles, C. A., Da Silva, A. M., Buchard, V., Colarco, P. R., Darmenov, A., Govindaraju, R., Smirnov, A., Holben, A., Ferrare, R., Hair, J., Shinozuka, Y. and Flynn, C. J.: The MERRA-2 aerosol reanalysis, 1980 onward. Part I: System description and data assimilation evaluation, J. Clim. 30(17), http://dx.doi.org/10.1175/ JCLI-D-16-0609.s1, 2017.

Rasch, P. J., Mahowald, N. M. and Eaton, B. E.: Representations of transport, convection, and the hydrologic cycle in chemical transport models: Implications for the modeling of short-lived and soluble species. J. of Geo. Res., 102, 127-138, 1997.

Rasch, P. J., Collins, W. D. and Eaton, B. E.: Understanding the Indian Ocean Experiment (INDOEX) aerosol distributions with an aerosol assimilation. J. of Geo. Res., 106, 7337-7355, 2001.

Remer, L. A., and Co-authors: The MODIS aerosol algorithm, products, and validation. J. Atmos. Sci., 62, 947–973, 2005.

823 Remer, L. A., Kleidman, R. G., Levy, R. C., Kaufman, Y. J., Tanre, D., Mattoo, S.,
824 Vanderlei Martins, J., Ichoku, C., Koren, I., Yu, H. and Holben, B. N.: Global aerosol
825 climatology from the MODIS satellite sensors. J. Geophys. Res.: A. 113(D14),
826 https://doi.org/10.1029/2007JD009661, 2008.
827 Rose, F. G, Rutan, D. A., Charlock, T., Smith, G. L. and Kato, S.: An Algorithm for the
828 Constraining of Radiative Transfer Calculations to CERES-Observed Broadband
829 Top-of-Atmosphere Irradiance. J. Atmos. and Ocean. Tech. 30, 1091-1106. DOI:
830 10.1175/JTECH-D-12-00058.1, 2013.
831 Rutan, D., Rose, F., Roman, M., Manalo-Smith, N., Schaaf, C. and Charlock, T.:
832 Development and assessment of broadband surface albedo from Clouds and the
833 Earth's Radiant Energy System clouds and radiation swath data product. J. Geophys.
834 Res., 114, D08125. doi:10.1029/2008JD010669, 2009.
835 Rutan, D., Kato, S., Doelling, D. R., Rose, F. G., Nguyen, L. T. and Caldwell, T.: CERES
836 Synoptic Product: Methodology and Validation of Surface Radiant Flux. J. Atmos.
837 And Ocean. Tech., 32, doi:10.1175/JTECH-D-14-00165.1, 2015.
838 Servain, J., Busalacchi, A. J., McPhaden, M. J., Moura, A. D., Reverdin, G., Vianna, M.
839 and Zebiak, S. E.: A Pilot Research Moored Array in the Tropical Atlantic
840 (PIRATA). Bull. Amer. Meteor. Soc., 79, 2019–2031, doi:10.1175/ 1520-
841 0477(1998)079,2019:APRMAI.2.0.CO;2. 1998
842 Sinyuk, A., Torres, O. and Dubovik, O.: Combined use of satellite and surface
843 observations to infer the imaginary part of refractive index of Saharan dust.
844 Geophysical Research Letters, 30(2), 1081. https://doi.org/10.1029/2002GL016189,
845 2003.

Smirnov, A., Holben, B. N., Eck, T. F., Dubovik, O. and Slutsker, I.: Cloud-screening and quality control algorithms for the AERONET database. Rem. Sens. Env. 73, 337-349, 2000.

Soden, B. and Chung, E-S.: The Large-Scale Dynamical Response of Clouds to Aerosol Forcing. J. of Climate, 30, 8783-8794. doi: https://doi.org/10.1175/JCLI-D-17-0050.1, 2017.

Stephens, G. L., Slingo, J. M., Rignot, E., Reager, J. T., Hakuba, M. Z., Durack, P. J., Worden, J. and Rocca, R.: Earth's water reservoirs in a changing climate. Proc. R. Soc. A 476: 20190458. http://dx.doi.org/10.1098/rspa.2019.0458, 2020.

Su, W., Schuster, G. L., Loeb, N. G., Rogers, R. R., Ferrare, R. A., Hostetler, C. A., Hair, J. W., and Obland, M. D.: Aerosol and cloud interaction observed from high spectral resolution lidar data. J. of Geophys. Res.: Atmos., 113(D24), D24202. Doi:10.1029/2008JD010588, 2008.

Su, W., Corbett, J., Eitzen, Z. and Liang, L.: Next-generation angular distribution models for top-of-atmosphere radiative flux calculation from CERES instruments: methodology. Atmos. Meas. Tech., 8(2), 611-632. doi: 10.5194/amt-8-611-2015, 2015.

Su, W., Corbett, J., Eitzen, Z. and Liang, L.: Next-generation angular distribution models for top-of-atmosphere radiative flux calculation from CERES instruments: validation. Atmos. Meas. Tech., 8(8), 3297-3313. doi: 10.5194/amt-8-3297-2015, 2015.

Su, W., G. L. Schuster, N. G. Loeb, R. R. Rogers, R. A. Ferrare, C. A. Hostetler, J. W. Hair, M. D. Obland, 2008: Aerosol and cloud interaction observed from high spectral

resolution lidar data. J. of Geophy. Res,: Atmos., 113(D24), D24202. Doi:10.1029/2008JD010588.

Textor, C. and Co-authors: Analysis and quantification of the diversities of aerosol life cycles within AeroCom, Atmos. Chem. Phys., 6, 1777-1813. www.atmos-chem-phys.net/6/1777/2006/, 2006.

Textor, C., and Co-authors: The effect of harmonized emissions on aerosol properties in global models – an AeroCom experiment. Atmos. Chem. Phys., 7, 4489–4501. www.atmos-chem-phys.net/7/4489/2007/, 2007.

Varnai, T., Marshak, A. and Eck, T. F.: Observation-based study on aerosol optical depth and particle size in partly cloudy regions. J. Geophys. Res: A. 122, 10,013–10,024, https://doi.org/10.1002/2017JD027028, 2017.

Wen, G., Marshak, A., Cahalan, R. F., Remer, L. A. and Kleidman, R. G.: 3-D aerosol-cloud radiative interaction observed in collocated MODIS and ASTER images of cumulus cloud fields, J. Geophys. Res., 112, D13204, doi:10.1029/2006JD008267, 2007.

Wielicki, B. A., Barkstrom, B. R., Harrison, E. F., Lee, R. B. III, Smith, G. L. and Cooper, J. E.: Clouds and the Earth's Radiant Energy System (CERES): An Earth Observing System Experiment. Bull. Amer. Meteor. Soc., 77, 853-868, 1996.

Zender, C. S., Huishen, B. and Newman, D.: Mineral Dust Entrainment and Deposition (DEAD) model: Description and 1990s dust climatology. J. Geophys. Res., 108, doi:10.1029/2002JD002775, 2003.